Numerical Study of Dissipative Weak Solutions for the Euler Equations of Gas Dynamics

Shaoshuai Chu,* Michael Herty,† Alexander Kurganov,‡ Mária Lukáčová-Medviďová,§ and Changsheng Yu¶

Abstract

We study dissipative weak (DW) solutions of the Euler equations of gas dynamics using the first-, second-, third-, fifth-, seventh-, and ninth-order local characteristic decomposition-based central-upwind (LCDCU), low-dissipation central-upwind (LDCU), and viscous finite volume (VFV) methods, whose higher-order extensions are obtained via the framework of the alternative weighted essentially non-oscillatory (A-WENO) schemes. These methods are applied to several benchmark problems, including several two-dimensional Riemann problems and a Kelvin–Helmholtz instability test. The numerical results demonstrate that for methods converging only weakly in space and time, the limiting solutions are generalized DW solutions, approximated in the sense of $\mathcal{K}$-convergence and dependent on the numerical scheme. For all of the studied methods, we compute the associated Young measures and compare the DW solutions using entropy production and energy defect criteria.

Key words: Dissipative solutions; Euler equations of gas dynamics; finite volume methods; high-order schemes; two-dimensional Riemann problems; Kelvin-Helmholtz instability.

AMS subject classification: 65M08, 65M12, 76M12, 76M20, 76N10, 35L65.

1 Introduction

We consider the two-dimensional (2-D) Euler equations of gas dynamics, which read as

$$
\begin{aligned}
&\rho_t + (\rho u)_x + (\rho v)_y = 0, \\
&(\rho u)_t + (\rho u^2 + p)_x + (\rho uv)_y = 0, \\
&(\rho v)_t + (\rho uv)_x + (\rho v^2 + p)_y = 0, \\
&E_t + [u(E + p)]_x + [v(E + p)]_y = 0.
\end{aligned}
\tag{1.1}
$$

Here, x and y are spatial variables, t the time, ρ is the density, u and v are the velocities in the x- and y-directions, respectively, E is the total energy, p is the pressure. The system (1.1) is closed using the following polytropic equation of state:

$$
e(\rho, \theta) = c_v \theta, \ c_v = \frac{1}{\gamma - 1}, \quad p(\rho, \theta) = (\gamma - 1)\rho e = \rho\theta = (\gamma - 1)\Big[E - \frac{1}{2}\rho(u^2 + v^2)\Big],
\tag{1.2}
$$

---

*Department of Mathematics, RWTH Aachen University, 52056 Aachen, Germany; `chu@igpm.rwth-aachen.de`

†Department of Mathematics, RWTH Aachen University, 52056 Aachen, Germany; Department of Mathematics and Applied Mathematics, University of Pretoria, Hatfield, 0028, South Africa; `herty@igpm.rwth-aachen.de`

‡Department of Mathematics and Shenzhen International Center for Mathematics, Southern University of Science and Technology, Shenzhen, 518055, China; `alexander@sustech.edu.cn`

§Institute of Mathematics, Johannes Gutenberg-University Mainz, 55128 Mainz, Germany; `lukacova@uni-mainz.de`

¶Institute of Mathematics, Johannes Gutenberg-University Mainz, 55128 Mainz, Germany; `chayu@uni-mainz.de`

where e is the specific internal energy, θ is the absolute temperature, $\boldsymbol{m} = (\rho u, \rho v)^\top$ is the momentum vector, and $\gamma > 1$ is a constant representing the adiabatic coefficient. The second law of thermodynamics is expressed by the entropy inequality for the total entropy S:

$$S_t + (Su)_x + (Sv)_y \geq 0, \quad S := c_v \rho \ln\left(\frac{p}{\rho^\gamma}\right). \tag{1.3}$$

We consider a bounded domain $\Omega \subset \mathbb{R}^2$, with either periodic or no-flux boundary conditions, and the initial conditions

$$\rho(x, y, 0) = \rho_0(x, y), \quad \boldsymbol{m}(x, y, 0) = \boldsymbol{m}_0(x, y), \quad S(x, y, 0) = S_0(x, y), \quad E_0 = \rho_0 e(\rho_0, S_0) + \frac{|\boldsymbol{m}_0|^2}{2\rho_0}. \tag{1.4}$$

It is well-known that solutions of (1.1)–(1.2) may develop complex wave structures, such as shock waves, rarefactions, and contact discontinuities, even when the initial data are infinitely smooth. Consequently, distributional weak solutions of (1.1)–(1.2) are typically considered. However, it was proved in [12] that the multidimensional compressible Euler equations admit infinitely many weak entropy solutions satisfying (1.3) for a wide range of initial data; see also [2, 7, 15] and references therein.

As it was demonstrated in many simulations reported in, e.g., [4,5,16,21,27], no strong convergence is observed when numerical methods are applied to shear flows appearing, for instance, in Kelvin-Helmholtz (KH) instability problems. Consequently, a natural question arises: *What is the weak limit of those numerical approximations?* To answer this question, one has to introduce a generalized solution concept, which is amenable to numerical methods. As advocated in [13], measure-valued solutions are suitable to represent low-regularity or rough solutions. Measure-valued solutions for multidimensional hyperbolic conservation laws were also studied in [21] and references therein. In this paper, we will concentrate on consistent approximations of dissipative weak (DW) solutions [19] of the Euler equations of gas dynamics.

According to the results reported in [16,21], the limit of consistent approximations is not a weak solution in the sense of distributions, if the convergence is only weak. However, a weak convergence of numerical solutions can lead to the strong convergence to a DW solution by averaging the numerical solutions over different mesh resolutions. In [19,30], the Cesàro averages over different meshes were considered for low-order numerical methods and a strong convergence of the Cesàro averages to a DW solution was observed; see also [16] as well as [6], where a fifth-order alternative weighted essentially non-oscillatory (A-WENO) scheme was used to compute the Cesàro averages.

In this paper, we study the convergence of several modern finite volume (FV) and finite difference (FD) methods of different orders of spatial accuracy. Although a rigorous consistency analysis is not available for high-order methods, the numerical study presented in this paper indicates that the numerical approximations of different orders converge weakly. This demonstrates that the consistency errors decay when the mesh is refined. The sequence of numerical solutions behaves in the following way. When a weak solution of the problem exists, all different numerical methods converge to this weak solution. However, when the solutions exhibit oscillations and develop turbulent structures, different numerical methods may yield different limiting DW solutions. In light of this observation, we discuss possible selection criteria for choosing an admissible and physically relevant solution among those oscillatory numerical solutions.

The paper is organized as follows. In §2, we give a brief overview of consistent approximations and DW solutions. In §3, we present a description of FV and FD methods used in the conducted numerical experiments. §4 contains simulations for several problems, including several configurations of the 2-D Riemann problems and the KH instability. We analyze the density profiles of the obtained numerical solutions, along with the averages over solutions of different orders and their time averages. For the KH problem, we also compute the underlying Young measure in specific subdomains. Additionally, we assess entropy production and energy defects of various methods to evaluate them with respect to the selection criteria. Finally, §5 is devoted to a brief conclusion.

2 Consistent Approximations and Dissipative Weak Solutions

To analyze a given numerical method and establish its convergence, it is essential to investigate the local consistency error. For this purpose, the notion of a consistent approximation seems to be particularly useful; see, e.g., [19].

Definition 2.1 (Consistent approximation) *A sequence $\{\rho_\ell, \boldsymbol{m}_\ell, S_\ell\}_{\ell=1}^\infty$ is a consistent approximation of (1.1)–(1.4) in $\Omega \times (0,T)$ if*

• *There is a sequence $\{\rho_{0,\ell}, \boldsymbol{m}_{0,\ell}, S_{0,\ell}\}_{\ell=1}^\infty$, that weakly approximates the initial data (1.4), that is,*

$$\rho_{0,\ell} \to \rho_0 \ \text{weakly in } L^1(\Omega), \quad \boldsymbol{m}_{0,\ell} \to \boldsymbol{m}_0 \ \text{weakly in } L^1(\Omega; \mathbb{R}^2), \quad S_{0,\ell} \to S_0 \ \text{weakly in } L^1(\Omega),$$

$$\int_\Omega \left(\frac{|\boldsymbol{m}_{0,\ell}|^2}{2\rho_{0,\ell}} + \rho_{0,\ell} e(\rho_{0,\ell}, S_{0,\ell}) \right) \mathrm{d}x\mathrm{d}y \to \int_\Omega \left(\frac{|\boldsymbol{m}_0|^2}{2\rho_0} + \rho_0 e(\rho_0, S_0) \right) \mathrm{d}x\mathrm{d}y,$$

and satisfies the **energy inequality**

$$\int_\Omega \left(\frac{|\boldsymbol{m}_\ell|^2}{2\rho_\ell} + \rho_\ell e(\rho_\ell, S_\ell) \right)(\cdot, t)\, \mathrm{d}x\mathrm{d}y \le \int_\Omega \left(\frac{|\boldsymbol{m}_{0,\ell}|^2}{2\rho_{0,\ell}} + \rho_{0,\ell} e(\rho_{0,\ell}, S_{0,\ell}) \right) \mathrm{d}x\mathrm{d}y + e_\ell^1$$

for a.a. $t \in [0,T]$ with $e_\ell^1 \to 0$ as $\ell \to \infty$;

• *The* **equation of continuity**

$$\int_0^T \int_\Omega (\rho_\ell \varphi_t + \boldsymbol{m}_\ell \cdot \nabla\varphi)\, \mathrm{d}x\mathrm{d}y\mathrm{d}t = -\int_\Omega \rho_{0,\ell} \varphi(\cdot, 0)\, \mathrm{d}x\mathrm{d}y + e_\ell^2[\varphi]$$

holds for any $\varphi \in C_c^1(\Omega \times [0,T))$ with $e_\ell^2[\varphi] \to 0$ as $\ell \to \infty$ for any $\varphi \in C_c^2(\Omega \times [0,T))$;

• *The* **momentum equation**

$$\int_0^T \int_\Omega \left(\boldsymbol{m}_\ell \cdot \boldsymbol{\varphi}_t + \mathbb{1}_{\rho_\ell > 0} \frac{\boldsymbol{m}_\ell \otimes \boldsymbol{m}_\ell}{\rho_\ell} : \boldsymbol{\nabla}\boldsymbol{\varphi} + \mathbb{1}_{\rho_\ell > 0} p(\rho_\ell, S_\ell) \boldsymbol{\nabla}\cdot\boldsymbol{\varphi} \right) \mathrm{d}x\mathrm{d}y\mathrm{d}t$$

$$= -\int_\Omega \boldsymbol{m}_{0,\ell} \boldsymbol{\varphi}(\cdot, 0)\, \mathrm{d}x\mathrm{d}y + e_\ell^3[\boldsymbol{\varphi}]$$

holds for any $\boldsymbol{\varphi} \in C_c^1(\Omega \times [0,T); \mathbb{R}^2)$ with $e_\ell^3[\boldsymbol{\varphi}] \to 0$ as $\ell \to \infty$ for any $\boldsymbol{\varphi} \in C_c^2(\Omega \times [0,T); \mathbb{R}^2)$;

• *The* **entropy inequality**

$$\int_0^T \int_\Omega \left(S_\ell \varphi_t + \mathbb{1}_{\rho_\ell > 0} \left(S_\ell \frac{\boldsymbol{m}_\ell}{\rho_\ell} \right) \cdot \nabla\varphi \right) \mathrm{d}x\mathrm{d}y\mathrm{d}t \le -\int_\Omega S_{0,\ell} \varphi(\cdot, 0) + e_\ell^4[\varphi]$$

holds for any $\varphi \in C_c^1(\Omega \times [0,T))$, $\varphi \ge 0$ with $e_\ell^4[\varphi] \to 0$ as $\ell \to \infty$ for any $\varphi \in C_c^2(\Omega \times [0,T))$;

• *The* **minimum entropy principle** *is satisfied, namely, there exists $\underline{s} \in \mathbb{R}$ such that $S_\ell \ge \rho_\ell \underline{s}$ a.e. in $\Omega \times (0,T)$.*

A consistent approximation can be obtained through various strategies, such as vanishing viscosity methods or structure-preserving numerical schemes. Different numerical methods on a sequence of refined meshes denoted as $\{\mathcal{I}_{h_n}\}_{n=1}^\infty$, where $h_n > 0$ represents a mesh parameter, were considered in [19]. This approach yields consistent approximations denoted by

$$\{\rho_\ell, \boldsymbol{m}_\ell, S_\ell\}_{\ell=1}^\infty = \{\rho_{h_n}, \boldsymbol{m}_{h_n}, S_{h_n}\}_{n=1}^\infty, \quad h_n \to 0 \text{ and } \ell = \ell(h_n) \to \infty \text{ as } n \to \infty.$$

The following result was established in [16].

Theorem 2.2 *Let $\{\rho_\ell, \boldsymbol{m}_\ell, S_\ell\}_{\ell=1}^\infty$ be a family of consistent approximations of (1.1)–(1.4) in the sense of Definition 2.1, such that*

$$\rho_\ell \to \rho \qquad \text{weakly-(*) in } L^\infty(0, T; L^\gamma(\Omega)),$$

$$\boldsymbol{m}_\ell \to \boldsymbol{m} \quad \text{weakly-(*) in } L^\infty(0, T; L^{\frac{2\gamma}{\gamma+1}}(\Omega; \mathbb{R}^2)),$$

$$S_\ell \to S \qquad \text{weakly-(*) in } L^\infty(0, T; L^\gamma(\Omega)),$$

as $\ell \to \infty$. Suppose that $S_\ell \geq \underline{s}\rho_\ell$ for some constant $\underline{s} \in \mathbb{R}$ uniformly for $\ell \to \infty$ and the limit $(\rho, \boldsymbol{m}, S)$ is a weak solution of (1.1)–(1.4). Then, for any finite $1 \leq r < \infty$, there exists a subsequence $\{\rho_{\ell_k}, \boldsymbol{m}_{\ell_k}, S_{\ell_k}\}$ such that

$$\rho_{\ell_k} \to \rho \qquad \text{in } L^r(0, T; L^\gamma(\Omega)),$$

$$\boldsymbol{m}_{\ell_k} \to \boldsymbol{m} \quad \text{in } L^r(0, T; L^{\frac{2\gamma}{\gamma+1}}(\Omega; \mathbb{R}^2)),$$

$$S_{\ell_k} \to S \qquad \text{in } L^r(0, T; L^\gamma(\Omega)),$$

as $\ell_k \to \infty$.

Next, we provide a definition of DW solutions and state two convergence results proved in [16, 18, 19].

Definition 2.3 (DW solution) *Let the initial data satisfy*

$$\rho_0 \in L^\gamma(\Omega), \quad \boldsymbol{m}_0 \in L^{\frac{2\gamma}{\gamma+1}}(\Omega; \mathbb{R}^2), \quad S_0 \in L^\gamma(\Omega), \quad \text{and} \quad \int_\Omega E(\rho_0, \boldsymbol{m}_0, S_0)\, \mathrm{d}x\mathrm{d}y < \infty,$$

We say that $(\rho, \boldsymbol{m}, S)$ is a DW solution of (1.1)–(1.4) in $\Omega \times [0, T]$, $0 < T \leq \infty$, if it satisfies the following properties.

- **Regularity**

$$\rho \in C_{\text{weak}}([0, T]; L^\gamma(\Omega)), \quad \boldsymbol{m} \in C_{\text{weak}}([0, T]; L^{\frac{2\gamma}{\gamma+1}}(\Omega; \mathbb{R}^2)),$$
$$S \in L^\infty(0, T; L^\gamma(\Omega)) \cap BV_{\text{weak}}([0, T]; L^\gamma(\Omega)),$$
$$\int_\Omega E(\rho, \boldsymbol{m}, S)(\cdot, t)\, \mathrm{d}x\mathrm{d}y \leq \int_\Omega E(\rho_0, \boldsymbol{m}_0, S_0)\, \mathrm{d}x\mathrm{d}y \quad \text{for any } t \in [0, T].$$

- *The* **equation of continuity**

$$\int_0^T \int_\Omega (\rho\varphi_t + \boldsymbol{m}\cdot\nabla\varphi)\, \mathrm{d}x\mathrm{d}y\mathrm{d}t = -\int_\Omega \rho_0\varphi(\cdot, 0)\, \mathrm{d}x\mathrm{d}y$$

holds for any $\varphi \in C_c^1(\Omega \times [0, T))$.

- *The* **momentum equation**

$$\int_0^T \int_\Omega \left(\boldsymbol{m} \cdot \boldsymbol{\varphi}_t + \mathbb{1}_{\rho>0}\frac{\boldsymbol{m}\otimes\boldsymbol{m}}{\rho} : \boldsymbol{\nabla}\boldsymbol{\varphi} + p(\rho, S)\boldsymbol{\nabla}\cdot\boldsymbol{\varphi} \right) \mathrm{d}x\mathrm{d}y\mathrm{d}t$$

$$= -\int_0^T \int_\Omega \boldsymbol{\nabla}\boldsymbol{\varphi} : \mathrm{d}\mathfrak{R}(t)\, \mathrm{d}t - \int_\Omega \boldsymbol{m}_0 \cdot \boldsymbol{\varphi}(\cdot, 0)\, \mathrm{d}x\mathrm{d}y$$

holds for any $\boldsymbol{\varphi} \in C_c^1(\Omega \times [0, T); \mathbb{R}^2)$, where $\mathfrak{R} \in L^\infty(0, T; \mathcal{M}^+(\Omega; \mathbb{R}_{\text{sym}}^{2\times2}))$ is the Reynolds defect stress.

- *The **entropy inequality***

$$\int\limits_{\Omega}\Big[S(\cdot,\tau_2+)\varphi(\cdot,\tau_2+)-S(\cdot,\tau_1-)\varphi(\cdot,\tau_1-)\Big]\mathrm{d}x\mathrm{d}y\geq\int\limits_{\tau_1}^{\tau_2}\int\limits_{\Omega}\Big(S\varphi_t+\big\langle\mathcal{V}_{x,y,t};\mathbb{1}_{\widehat{\rho}>0}\big(\widehat{S}\widehat{u}\big)\big\rangle\cdot\nabla\varphi\Big)\mathrm{d}x\mathrm{d}y\mathrm{d}t,$$

with $S(\cdot,0-)=S_0$ holds for any $0\leq\tau_1\leq\tau_2<T$, any $\varphi\in C_c^1(\Omega\times[0,T))$, $\varphi\geq 0$, where $\{\mathcal{V}_{x,y,t}\}_{(x,y,t)\in\Omega\times(0,T)}$ is a parametrized probability (Young) measure:

$$\mathcal{V}_{x,y,t}\in L^\infty(\Omega\times(0,T));\mathcal{P}(\mathbb{R}^4)),\quad\mathbb{R}^4=\Big\{\widehat{\rho}\in\mathbb{R},\widehat{m}\in\mathbb{R}^2,\widehat{S}\in\mathbb{R}\Big\};$$
$$\langle\mathcal{V};\widehat{\rho}\rangle=\rho,\quad\langle\mathcal{V};\widehat{m}\rangle=m,\quad\langle\mathcal{V};\widehat{S}\rangle=S.$$

- *The **energy inequality** and compatibility of the energy and Reynolds stress defects.*

$$\int\limits_{\Omega}E\big(\rho(\cdot,t),m(\cdot,t),S(\cdot,t)\big)\,\mathrm{d}x\mathrm{d}y+\int\limits_{\overline{\Omega}}\mathrm{d}\mathfrak{E}(t)\leq\int\limits_{\Omega}E(\rho_0,m_0,S_0)\,\mathrm{d}x\mathrm{d}y,$$

where $\mathfrak{E}\in L^\infty(0,T;\mathcal{M}^+(\Omega))$ is the energy defect satisfying

$$2\min\big\{1,\gamma-1\big\}\,\mathfrak{E}\leq\mathrm{trace}[\mathfrak{R}]\leq 2\max\big\{1,\gamma-1\big\}\,\mathfrak{E}.$$

Remark 2.1 *A DW solution (ρ,m,S) can be interpreted as the expected value of a Young measure $\{\mathcal{V}_{x,y,t}\}$, which is generated by a consistent approximation of (1.1)–(1.4); see [19, Chapter 5]. Note that a dissipative-strong uniqueness principle for DW solutions holds. Consequently, as long as the strong solution exists, all DW solutions coincide with the strong solution.*

Theorem 2.4 (Weak versus strong convergence) *Let the initial data $\{\rho_{0,\ell},m_{0,\ell},E_{0,\ell}\}_{\ell=1}^\infty$ satisfy*

$$\rho_{0,\ell}>0,\quad E_{0,\ell}-\frac{|m_{0,\ell}|^2}{2\rho_{0,\ell}}>0,\quad\forall\ell.$$

Let $\{\rho_\ell,m_\ell,S_\ell\}_{\ell=1}^\infty$ be a consistent approximation of (1.1)–(1.4) in the sense of Definition 2.1 and let it be uniformly bounded, that is, there exists a positive constant C such that

$$\|(\rho_\ell,m_\ell,S_\ell)\|_{L^\infty(\Omega\times(0,T))}\leq C,\quad\forall\ell.$$

Then, a subsequence of the consistent approximation $\{\rho_{\ell_k},m_{\ell_k},S_{\ell_k}\}$ generates a DW solution (ρ,m,S) in the sense of Definition 2.3, that is,

$$(\rho_{\ell_k},m_{\ell_k},S_{\ell_k})\to(\rho,m,S)\ \ weakly\text{-}(*)\ in\ L^\infty(\Omega\times(0,T);\mathbb{R}^4),$$
$$E(\rho_{\ell_k},m_{\ell_k},S_{\ell_k})\to\big\langle\mathcal{V}_{x,y,t};E(\widehat{\rho},\widehat{m},\widehat{S})\big\rangle\ \ weakly\text{-}(*)\ in\ L^\infty(\Omega\times(0,T)),$$

as $\ell_k\to\infty$. Moreover, if the Euler system admits a strong solution (ρ,m,E), which is Lipschitz continuous in $\overline{\Omega}\times[0,T]$, then

$$\rho_\ell\to\rho,\quad m_\ell\to m,\quad E_\ell\to E\ \ in\ L^q(\overline{\Omega}\times(0,T))\ as\ \ell\to\infty,\ \forall q\in[1,\infty).$$

Theorem 2.5 ($\mathcal{K}$-convergence) *Let the assumptions of Theorem 2.4 hold and $\{\rho_\ell,m_\ell,S_\ell\}_{\ell=1}^\infty$ be a consistent and bounded approximation of (1.1)–(1.4). Then, there exists a subsequence $\{\rho_{\ell_k},m_{\ell_k},S_{\ell_k}\}$, which converges strongly to a DW solution (ρ,m,S) in the following sense:*

$$\big(\widetilde{\rho}_n,\widetilde{m}_n,\widetilde{S}_n\big):=\frac{1}{n}\sum_{k=1}^n(\rho_{\ell_k},m_{\ell_k},S_{\ell_k})\to(\rho,m,S)\ \ in\ L^q(\Omega\times(0,T);\mathbb{R}^4),\ \forall q\in[1,\infty),$$

$$\widetilde{E}_n:=\frac{1}{n}\sum_{k=1}^n E(\rho_{\ell_k},m_{\ell_k},S_{\ell_k})\to\big\langle\mathcal{V}_{x,y,t},E(\widehat{\rho},\widehat{m},\widehat{S})\big\rangle\ \ in\ L^q(\Omega\times(0,T)),\ \forall q\in[1,\infty),$$

as $n\to\infty$.

3   Numerical Schemes

In this section, we provide a brief overview of the 2-D semi-discrete schemes used to conduct the numerical experiments in this paper.

We introduce uniform rectangular cells $C_{j,k} := \left[x_{j-\frac{1}{2}}, x_{j+\frac{1}{2}}\right] \times \left[y_{k-\frac{1}{2}}, y_{k+\frac{1}{2}}\right]$ centered at (x_j, y_k) with $x_j = \left(x_{j-\frac{1}{2}} + x_{j+\frac{1}{2}}\right)/2$ and $y_k = \left(y_{k+\frac{1}{2}} + y_{k-\frac{1}{2}}\right)/2$. The spatial mesh sizes are $x_{j+\frac{1}{2}} - x_{j-\frac{1}{2}} \equiv \Delta x$ and $y_{k+\frac{1}{2}} - y_{k-\frac{1}{2}} \equiv \Delta y$, respectively. Below, we will describe low-order FV methods (§3.1) and high-order FD A-WENO schemes (§3.2).

In the FV methods, the computed discrete quantities are the cell averages, which are denoted by $\overline{U}_{j,k}(t) :\approx \frac{1}{\Delta x \Delta y} \int_{C_{j,k}} U(x, y, t)\, \mathrm{d}x \mathrm{d}y$ and assumed to be available at a certain time level t. Prior to evolving them in time, we will perform a conservative piecewise constant (for first-order methods) or piecewise linear (for second-order methods) reconstruction

$$\widetilde{U}(x, y) = \overline{U}_{j,k} + (U_x)_{j,k}(x - x_j) + (U_y)_{j,k}(y - y_k), \quad (x, y) \in C_{j,k}, \tag{3.1}$$

whose one-sided point values at the midpoints of the cell interfaces are

$$
\begin{aligned}
U_{j-\frac{1}{2},k}^{+} &= \overline{U}_{j,k} - \frac{\Delta x}{2}(U_x)_{j,k}, \quad U_{j+\frac{1}{2},k}^{-} = \overline{U}_{j,k} + \frac{\Delta x}{2}(U_x)_{j,k}, \\
U_{j,k-\frac{1}{2}}^{+} &= \overline{U}_{j,k} - \frac{\Delta y}{2}(U_y)_{j,k}, \quad U_{j,k+\frac{1}{2}}^{-} = \overline{U}_{j,k} + \frac{\Delta y}{2}(U_y)_{j,k},
\end{aligned}
\tag{3.2}
$$

where $(U_x)_{j,k} = (U_y)_{j,k} \equiv 0$ for all j, k for first-order methods, while for the second-order methods, the slopes $(U_x)_{j,k}$ and $(U_y)_{j,k}$ are to be computed using a nonlinear limiter. In the numerical results reported in §4, we have used a generalized minmod limiter (see, e.g., [28, 31, 37]):

$$
\begin{aligned}
(U_x)_{j,k} &= \mathrm{minmod}\left(\theta\, \frac{\overline{U}_{j+1,k} - \overline{U}_{j,k}}{\Delta x},\ \frac{\overline{U}_{j+1,k} - \overline{U}_{j-1,k}}{2\Delta x},\ \theta\, \frac{\overline{U}_{j,k} - \overline{U}_{j-1,k}}{\Delta x}\right), \\
(U_y)_{j,k} &= \mathrm{minmod}\left(\theta\, \frac{\overline{U}_{j,k+1} - \overline{U}_{j,k}}{\Delta y},\ \frac{\overline{U}_{j,k+1} - \overline{U}_{j,k-1}}{2\Delta y},\ \theta\, \frac{\overline{U}_{j,k} - \overline{U}_{j,k-1}}{\Delta y}\right),
\end{aligned}
\tag{3.3}
$$

where the minmod function is defined by

$$
\mathrm{minmod}(z_1, z_2, \dots) = \begin{cases} \min(z_1, z_2, \dots) & \text{if } z_i > 0, \forall i, \\ \max(z_1, z_2, \dots) & \text{if } z_i < 0, \forall i, \\ 0 & \text{otherwise}, \end{cases}
$$

and the parameter θ was set to 1.3.

Note that most of the indexed quantities in (3.1)–(3.3) as well as in formulae below are time-dependent, but we suppress this dependence for the sake of brevity.

In the FD A-WENO schemes, the computed discrete quantities are point values $U_{j,k} :\approx U(x_j, y_k, t)$. Before evolving them in time, we use one-dimensional WENO interpolants of an appropriate order, implemented in the local characteristic fields (see, e.g., [25, 29, 32, 33, 36] and references therein) in the x- and y-directions to obtain the point values $U_{j+\frac{1}{2},k}^{\pm}$ and $U_{j,k+\frac{1}{2}}^{\pm}$, respectively.

3.1   Low-Order FV Schemes

In these schemes, the cell averages $\overline{U}_{j,k}(t)$ are evolved in time by solving the following system of ODEs:

$$\frac{\mathrm{d}\overline{U}_{j,k}}{\mathrm{d}t} = -\frac{\mathcal{F}_{j+\frac{1}{2},k}^{\mathrm{FV}} - \mathcal{F}_{j-\frac{1}{2},k}^{\mathrm{FV}}}{\Delta x} - \frac{\mathcal{G}_{j,k+\frac{1}{2}}^{\mathrm{FV}} - \mathcal{G}_{j,k-\frac{1}{2}}^{\mathrm{FV}}}{\Delta y}, \tag{3.4}$$

where $\mathcal{F}_{j+\frac{1}{2},k}^{\mathrm{FV}}\left(U_{j+\frac{1}{2},k}^{-}, U_{j+\frac{1}{2},k}^{+}\right)$ and $\mathcal{G}_{j,k+\frac{1}{2}}^{\mathrm{FV}}\left(U_{j,k+\frac{1}{2}}^{-}, U_{j,k+\frac{1}{2}}^{+}\right)$ are either the local characteristic decomposition based central-upwind (LCDCU) numerical fluxes from [4], low-dissipation central-upwind

(LDCU) numerical fluxes from [10], or viscous finite volume (VFV) numerical fluxes from [19]. In the rest of this section, we provide a detailed description of the VFV numerical fluxes, which read as $\boldsymbol{\mathcal{F}}^{\mathrm{FV}}_{j+\frac{1}{2},k} = \big(\mathcal{F}^{\mathrm{FV},\rho}_{j+\frac{1}{2},k}, \mathcal{F}^{\mathrm{FV},\rho u}_{j+\frac{1}{2},k}, \mathcal{F}^{\mathrm{FV},\rho v}_{j+\frac{1}{2},k}, \mathcal{F}^{\mathrm{FV},E}_{j+\frac{1}{2},k}\big)$ and $\boldsymbol{\mathcal{G}}^{\mathrm{FV}}_{j,k+\frac{1}{2}} = \big(\mathcal{G}^{\mathrm{FV},\rho}_{j,k+\frac{1}{2}}, \mathcal{G}^{\mathrm{FV},\rho u}_{j,k+\frac{1}{2}}, \mathcal{G}^{\mathrm{FV},\rho v}_{j,k+\frac{1}{2}}, \mathcal{G}^{\mathrm{FV},E}_{j,k+\frac{1}{2}}\big)$, where

$$
\begin{aligned}
\mathcal{F}^{\mathrm{FV},\rho}_{j+\frac{1}{2},k} &= \mathcal{F}^{\mathrm{upw},\rho}_{j+\frac{1}{2},k}, \quad \mathcal{F}^{\mathrm{FV},\rho u}_{j+\frac{1}{2},k} = \mathcal{F}^{\mathrm{upw},\rho u}_{j+\frac{1}{2},k} + \frac{1}{2}\big(p^{-}_{j+\frac{1}{2},k} + p^{+}_{j+\frac{1}{2},k}\big) - \big(u^{+}_{j+\frac{1}{2},k} - u^{-}_{j+\frac{1}{2},k}\big), \\
\mathcal{F}^{\mathrm{FV},\rho v}_{j+\frac{1}{2},k} &= \mathcal{F}^{\mathrm{upw},\rho v}_{j+\frac{1}{2},k} - \big(v^{+}_{j+\frac{1}{2},k} - v^{-}_{j+\frac{1}{2},k}\big), \\
\mathcal{F}^{\mathrm{FV},E}_{j+\frac{1}{2},k} &= \mathcal{F}^{\mathrm{upw},E}_{j+\frac{1}{2},k} + \frac{1}{2}\big(u^{-}_{j+\frac{1}{2},k}p^{-}_{j+\frac{1}{2},k} + u^{+}_{j+\frac{1}{2},k}p^{+}_{j+\frac{1}{2},k}\big) \\
&\quad - \frac{1}{2}\Big(\big(u^{+}_{j+\frac{1}{2},k}\big)^2 + \big(v^{+}_{j+\frac{1}{2},k}\big)^2 - \big(u^{-}_{j+\frac{1}{2},k}\big)^2 - \big(v^{-}_{j+\frac{1}{2},k}\big)^2\Big),
\end{aligned}
\tag{3.5}
$$

and

$$
\begin{aligned}
\mathcal{G}^{\mathrm{FV},\rho}_{j,k+\frac{1}{2}} &= \mathcal{G}^{\mathrm{upw},\rho}_{j,k+\frac{1}{2}}, \quad \mathcal{G}^{\mathrm{FV},\rho u}_{j,k+\frac{1}{2}} = \mathcal{G}^{\mathrm{upw},\rho u}_{j,k+\frac{1}{2}} - \big(u^{+}_{j,k+\frac{1}{2}} - u^{-}_{j,k+\frac{1}{2}}\big), \\
\mathcal{G}^{\mathrm{FV},\rho v}_{j,k+\frac{1}{2}} &= \mathcal{G}^{\mathrm{upw},\rho v}_{j,k+\frac{1}{2}} + \frac{1}{2}\big(p^{-}_{j,k+\frac{1}{2}} + p^{+}_{j,k+\frac{1}{2}}\big) - \big(v^{+}_{j,k+\frac{1}{2}} - v^{-}_{j,k+\frac{1}{2}}\big), \\
\mathcal{G}^{\mathrm{FV},E}_{j,k+\frac{1}{2}} &= \mathcal{G}^{\mathrm{upw},E}_{j,k+\frac{1}{2}} + \frac{1}{2}\big(v^{-}_{j,k+\frac{1}{2}}p^{-}_{j,k+\frac{1}{2}} + v^{+}_{j,k+\frac{1}{2}}p^{+}_{j,k+\frac{1}{2}}\big) \\
&\quad - \frac{1}{2}\Big(\big(u^{+}_{j,k+\frac{1}{2}}\big)^2 + \big(v^{+}_{j,k+\frac{1}{2}}\big)^2 - \big(u^{-}_{j,k+\frac{1}{2}}\big)^2 - \big(v^{-}_{j,k+\frac{1}{2}}\big)^2\Big).
\end{aligned}
\tag{3.6}
$$

In the above formulae,

$$
\begin{aligned}
\boldsymbol{\mathcal{F}}^{\mathrm{upw}}_{j+\frac{1}{2},k} &= \frac{1}{4}\big(u^{-}_{j+\frac{1}{2},k} + u^{+}_{j+\frac{1}{2},k} - \big|u^{-}_{j+\frac{1}{2},k} + u^{+}_{j+\frac{1}{2},k}\big| - 4\big)\big(\boldsymbol{U}^{-}_{j+\frac{1}{2},k} + \boldsymbol{U}^{+}_{j+\frac{1}{2},k}\big), \\
\boldsymbol{\mathcal{G}}^{\mathrm{upw}}_{j,k+\frac{1}{2}} &= \frac{1}{4}\big(v^{-}_{j,k+\frac{1}{2}} + v^{+}_{j,k+\frac{1}{2}} - \big|v^{-}_{j,k+\frac{1}{2}} + v^{+}_{j,k+\frac{1}{2}}\big| - 4\big)\big(\boldsymbol{U}^{-}_{j,k+\frac{1}{2}} + \boldsymbol{U}^{+}_{j,k+\frac{1}{2}}\big),
\end{aligned}
\tag{3.7}
$$

$$
\begin{aligned}
u^{\pm}_{j+\frac{1}{2},k} &= \frac{(\rho u)^{\pm}_{j+\frac{1}{2},k}}{\rho^{\pm}_{j+\frac{1}{2},k}}, \quad v^{\pm}_{j+\frac{1}{2},k} = \frac{(\rho v)^{\pm}_{j+\frac{1}{2},k}}{\rho^{\pm}_{j+\frac{1}{2},k}}, \quad p^{\pm}_{j+\frac{1}{2},k} = (\gamma - 1)\left[E^{\pm}_{j+\frac{1}{2},k} - \frac{\big((\rho u)^{\pm}_{j+\frac{1}{2},k}\big)^2 + \big((\rho v)^{\pm}_{j+\frac{1}{2},k}\big)^2}{2\rho^{\pm}_{j+\frac{1}{2},k}}\right], \\
u^{\pm}_{j,k+\frac{1}{2}} &= \frac{(\rho u)^{\pm}_{j,k+\frac{1}{2}}}{\rho^{\pm}_{j,k+\frac{1}{2}}}, \quad v^{\pm}_{j,k+\frac{1}{2}} = \frac{(\rho v)^{\pm}_{j,k+\frac{1}{2}}}{\rho^{\pm}_{j,k+\frac{1}{2}}}, \quad p^{\pm}_{j,k+\frac{1}{2}} = (\gamma - 1)\left[E^{\pm}_{j,k+\frac{1}{2}} - \frac{\big((\rho u)^{\pm}_{j,k+\frac{1}{2}}\big)^2 + \big((\rho v)^{\pm}_{j,k+\frac{1}{2}}\big)^2}{2\rho^{\pm}_{j,k+\frac{1}{2}}}\right].
\end{aligned}
$$

Remark 3.1 *We stress that the first-order VFV scheme, which according to [18] produces consistent approximations, is slightly different from the scheme (3.4)–(3.7). The difference is in the evolution of $\overline{E}_{j,k}$, which, in the first-order scheme, reads as*

$$
\begin{aligned}
\frac{\mathrm{d}\overline{E}_{j,k}}{\mathrm{d}t} &= -\frac{\mathcal{F}^{\mathrm{upw},E}_{j+\frac{1}{2},k} - \mathcal{F}^{\mathrm{upw},E}_{j-\frac{1}{2},k}}{\Delta x} - \frac{\mathcal{G}^{\mathrm{upw},E}_{j,k+\frac{1}{2}} - \mathcal{G}^{\mathrm{upw},E}_{j,k-\frac{1}{2}}}{\Delta y} \\
&\quad - u_{j,k}\frac{p_{j+1,k} - p_{j-1,k}}{2\Delta x} - p_{j,k}\frac{u_{j+1,k} - u_{j-1,k}}{2\Delta x} - v_{j,k}\frac{p_{j,k+1} - p_{j,k-1}}{2\Delta y} - p_{j,k}\frac{v_{j,k+1} - v_{j,k-1}}{2\Delta y} \\
&\quad + \frac{(u^{+}_{j+1,k})^2 - 2(u^{+}_{j,k})^2 + (u^{+}_{j-1,k})^2 + (v^{+}_{j+1,k})^2 - 2(v^{+}_{j,k})^2 + (v^{+}_{j-1,k})^2}{2\Delta x} \\
&\quad + \frac{(u^{+}_{j,k+1})^2 - 2(u^{+}_{j,k})^2 + (u^{+}_{j,k-1})^2 + (v^{+}_{j,k+1})^2 - 2(v^{+}_{j,k})^2 + (v^{+}_{j,k-1})^2}{2\Delta y}.
\end{aligned}
$$

3.2 High-Order FD A-WENO Schemes

In this section, we present higher-order extensions of the low-order schemes from §3.1 within the FD A-WENO framework introduced in [25]; see also [11, 22, 29].

In FD A-WENO schemes, computed solutions are realized in terms of the point values $\boldsymbol{U}_{j,k}$ (rather than the cell averages $\overline{\boldsymbol{U}}_{j,k}$), which are evolved in time by solving the following system of ODEs:

$$\frac{\mathrm{d}\boldsymbol{U}_{j,k}}{\mathrm{d}t} = -\frac{\boldsymbol{\mathcal{F}}_{j+\frac{1}{2},k} - \boldsymbol{\mathcal{F}}_{j-\frac{1}{2},k}}{\Delta x} - \frac{\boldsymbol{\mathcal{G}}_{j,k+\frac{1}{2}} - \boldsymbol{\mathcal{G}}_{j,k-\frac{1}{2}}}{\Delta y}, \tag{3.8}$$

where the numerical fluxes $\boldsymbol{\mathcal{F}}_{j+\frac{1}{2},k}$ and $\boldsymbol{\mathcal{G}}_{j,k+\frac{1}{2}}$ are defined by

$$\begin{aligned}
\boldsymbol{\mathcal{F}}_{j+\frac{1}{2},k} &= \boldsymbol{\mathcal{F}}_{j+\frac{1}{2},k}^{\mathrm{FV}} - \mu_2(\Delta x)^2(\boldsymbol{F}_{xx})_{j+\frac{1}{2},k} + H(r-4)\mu_4(\Delta x)^4(\boldsymbol{F}_{xxxx})_{j+\frac{1}{2},k} \\
&\quad - H(r-6)\mu_6(\Delta x)^6(\boldsymbol{F}_{xxxxxx})_{j+\frac{1}{2},k} + H(r-8)\mu_8(\Delta x)^8(\boldsymbol{F}_{xxxxxxxx})_{j+\frac{1}{2},k}, \\
\boldsymbol{\mathcal{G}}_{j,k+\frac{1}{2}} &= \boldsymbol{\mathcal{G}}_{j,k+\frac{1}{2}}^{\mathrm{FV}} - \mu_2(\Delta y)^2(\boldsymbol{G}_{yy})_{j,k+\frac{1}{2}} + H(r-4)\mu_4(\Delta y)^4(\boldsymbol{G}_{yyyy})_{j,k+\frac{1}{2}} \\
&\quad - H(r-6)\mu_6(\Delta y)^6(\boldsymbol{G}_{yyyyyy})_{j,k+\frac{1}{2}} + H(r-8)\mu_8(\Delta y)^8(\boldsymbol{G}_{yyyyyyyy})_{j,k+\frac{1}{2}}.
\end{aligned}$$

Here, $\mu_2 = 1/24$, $\mu_4 = 7/5760$, $\mu_6 = 31/967680$, $\mu_8 = 127/154828800$, H is the Heaviside function, $r = 3, 5, 7$, or 9 is the order of the scheme, $\boldsymbol{\mathcal{F}}_{j+\frac{1}{2},k}^{\mathrm{FV}}\big(\boldsymbol{U}_{j+\frac{1}{2},k}^-, \boldsymbol{U}_{j+\frac{1}{2},k}^+\big)$ and $\boldsymbol{\mathcal{G}}_{j,k+\frac{1}{2}}^{\mathrm{FV}}\big(\boldsymbol{U}_{j,k+\frac{1}{2}}^-, \boldsymbol{U}_{j,k+\frac{1}{2}}^+\big)$ are the FV numerical fluxes, which are computed using the one-sided point values $\boldsymbol{U}_{j+\frac{1}{2},k}^{\pm}$, which are obtained using an rth-order WENO interpolation applied to the local characteristic variables, and $(\boldsymbol{F}_{xx})_{j+\frac{1}{2},k}$, $(\boldsymbol{F}_{xxxx})_{j+\frac{1}{2},k}$, $(\boldsymbol{F}_{xxxxxx})_{j+\frac{1}{2},k}$, $(\boldsymbol{F}_{xxxxxxxx})_{j+\frac{1}{2},k}$, $(\boldsymbol{G}_{yy})_{j,k+\frac{1}{2}}$, $(\boldsymbol{G}_{yyyy})_{j,k+\frac{1}{2}}$, $(\boldsymbol{G}_{yyyyyy})_{j,k+\frac{1}{2}}$, and $(\boldsymbol{G}_{yyyyyyyy})_{j,k+\frac{1}{2}}$ are the higher-order correction terms, which can be computed with the help of the FV numerical fluxes $\boldsymbol{\mathcal{F}}_{j+\frac{1}{2},k}^{\mathrm{FV}}$ and $\boldsymbol{\mathcal{G}}_{j,k+\frac{1}{2}}^{\mathrm{FV}}$ as it was first done in [11] for the fifth-order A-WENO schemes. The formulae for these terms depend on the order of the scheme and for different values of r they are given below together with the details on particular WENO interpolations used for each r.

$r = 3$ (third-order schemes)

$$(\boldsymbol{F}_{xx})_{j+\frac{1}{2},k} = \frac{1}{(\Delta x)^2}\Big[\boldsymbol{\mathcal{F}}_{j-\frac{1}{2},k}^{\mathrm{FV}} - 2\boldsymbol{\mathcal{F}}_{j+\frac{1}{2},k}^{\mathrm{FV}} + \boldsymbol{\mathcal{F}}_{j+\frac{3}{2},k}^{\mathrm{FV}}\Big], \quad (\boldsymbol{G}_{yy})_{j,k+\frac{1}{2}} = \frac{1}{(\Delta y)^2}\Big[\boldsymbol{\mathcal{G}}_{j,k-\frac{1}{2}}^{\mathrm{FV}} - 2\boldsymbol{\mathcal{G}}_{j,k+\frac{1}{2}}^{\mathrm{FV}} + \boldsymbol{\mathcal{G}}_{j,k+\frac{3}{2}}^{\mathrm{FV}}\Big].$$

The one-sided point values $\boldsymbol{U}_{j+\frac{1}{2},k}^{\pm}$ and $\boldsymbol{U}_{j,k+\frac{1}{2}}^{\pm}$ are computed using the third-order WENO interpolation introduced in [8,9]; for details, we refer the reader to [9, Appendix A].

$r = 5$ (fifth-order schemes) $(\boldsymbol{F}_{xx})_{j+\frac{1}{2},k}$, $(\boldsymbol{F}_{xxxx})_{j+\frac{1}{2},k}$, $(\boldsymbol{G}_{yy})_{j,k+\frac{1}{2}}$, and $(\boldsymbol{G}_{yyyy})_{j,k+\frac{1}{2}}$ are defined in [11, (4.4)], and the one-sided point values $\boldsymbol{U}_{j+\frac{1}{2},k}^{\pm}$ and $\boldsymbol{U}_{j,k+\frac{1}{2}}^{\pm}$ are computed using the fifth-order WENO-Z interpolation from [1,3,14]; for details, we refer the reader to [5, Appendix A].

$r = 7$ (seventh-order schemes)

$$\begin{aligned}
(\boldsymbol{F}_{xx})_{j+\frac{1}{2},k} &= \frac{1}{180(\Delta x)^2}\Big[2\boldsymbol{\mathcal{F}}_{j-\frac{5}{2},k}^{\mathrm{FV}} - 27\boldsymbol{\mathcal{F}}_{j-\frac{3}{2},k}^{\mathrm{FV}} + 270\boldsymbol{\mathcal{F}}_{j-\frac{1}{2},k}^{\mathrm{FV}} \\
&\quad - 490\boldsymbol{\mathcal{F}}_{j+\frac{1}{2},k}^{\mathrm{FV}} + 270\boldsymbol{\mathcal{F}}_{j+\frac{3}{2},k}^{\mathrm{FV}} - 27\boldsymbol{\mathcal{F}}_{j+\frac{5}{2},k}^{\mathrm{FV}} + 2\boldsymbol{\mathcal{F}}_{j+\frac{7}{2},k}^{\mathrm{FV}}\Big], \\
(\boldsymbol{F}_{xxxx})_{j+\frac{1}{2},k} &= \frac{1}{6(\Delta x)^4}\Big[-\boldsymbol{\mathcal{F}}_{j-\frac{5}{2},k}^{\mathrm{FV}} + 12\boldsymbol{\mathcal{F}}_{j-\frac{3}{2},k}^{\mathrm{FV}} - 39\boldsymbol{\mathcal{F}}_{j-\frac{1}{2},k}^{\mathrm{FV}} \\
&\quad + 56\boldsymbol{\mathcal{F}}_{j+\frac{1}{2},k}^{\mathrm{FV}} - 39\boldsymbol{\mathcal{F}}_{j+\frac{3}{2},k}^{\mathrm{FV}} + 12\boldsymbol{\mathcal{F}}_{j+\frac{5}{2},k}^{\mathrm{FV}} - \boldsymbol{\mathcal{F}}_{j+\frac{7}{2},k}^{\mathrm{FV}}\Big], \\
(\boldsymbol{F}_{xxxxxx})_{j+\frac{1}{2},k} &= \frac{1}{(\Delta x)^6}\Big[\boldsymbol{\mathcal{F}}_{j-\frac{5}{2},k}^{\mathrm{FV}} - 6\boldsymbol{\mathcal{F}}_{j-\frac{3}{2},k}^{\mathrm{FV}} + 15\boldsymbol{\mathcal{F}}_{j-\frac{1}{2},k}^{\mathrm{FV}} \\
&\quad - 20\boldsymbol{\mathcal{F}}_{j+\frac{1}{2},k}^{\mathrm{FV}} + 15\boldsymbol{\mathcal{F}}_{j+\frac{3}{2},k}^{\mathrm{FV}} - 6\boldsymbol{\mathcal{F}}_{j+\frac{5}{2},k}^{\mathrm{FV}} + \boldsymbol{\mathcal{F}}_{j+\frac{7}{2},k}^{\mathrm{FV}}\Big], \\
(\boldsymbol{G}_{yy})_{j,k+\frac{1}{2}} &= \frac{1}{180(\Delta y)^2}\Big[2\boldsymbol{\mathcal{G}}_{j,k-\frac{5}{2}}^{\mathrm{FV}} - 27\boldsymbol{\mathcal{G}}_{j,k-\frac{3}{2}}^{\mathrm{FV}} + 270\boldsymbol{\mathcal{G}}_{j,k-\frac{1}{2}}^{\mathrm{FV}}
\end{aligned}$$

$$- 490\boldsymbol{\mathcal{G}}^{\mathrm{FV}}_{j,k+\frac{1}{2}} + 270\boldsymbol{\mathcal{G}}^{\mathrm{FV}}_{j,k+\frac{3}{2}} - 27\boldsymbol{\mathcal{G}}^{\mathrm{FV}}_{j,k+\frac{5}{2}} + 2\boldsymbol{\mathcal{G}}^{\mathrm{FV}}_{j,k+\frac{7}{2}}\Big],$$

$$(\boldsymbol{G}_{yyyy})_{j,k+\frac{1}{2}} = \frac{1}{6(\Delta y)^4}\Big[-\boldsymbol{\mathcal{G}}^{\mathrm{FV}}_{j,k-\frac{5}{2}} + 12\boldsymbol{\mathcal{G}}^{\mathrm{FV}}_{j,k-\frac{3}{2}} - 39\boldsymbol{\mathcal{G}}^{\mathrm{FV}}_{j,k-\frac{1}{2}}$$
$$+ 56\boldsymbol{\mathcal{G}}^{\mathrm{FV}}_{j,k+\frac{1}{2}} - 39\boldsymbol{\mathcal{G}}^{\mathrm{FV}}_{j,k+\frac{3}{2}} + 12\boldsymbol{\mathcal{G}}^{\mathrm{FV}}_{j,k+\frac{5}{2}} - \boldsymbol{\mathcal{G}}^{\mathrm{FV}}_{j,k+\frac{7}{2}}\Big],$$

$$(\boldsymbol{G}_{yyyyyy})_{j,k+\frac{1}{2}} = \frac{1}{(\Delta y)^6}\Big[\boldsymbol{\mathcal{G}}^{\mathrm{FV}}_{j,k-\frac{5}{2}} - 6\boldsymbol{\mathcal{G}}^{\mathrm{FV}}_{j,k-\frac{3}{2}} + 15\boldsymbol{\mathcal{G}}^{\mathrm{FV}}_{j,k-\frac{1}{2}} - 20\boldsymbol{\mathcal{G}}^{\mathrm{FV}}_{j,k+\frac{1}{2}} + 15\boldsymbol{\mathcal{G}}^{\mathrm{FV}}_{j,k+\frac{3}{2}} - 6\boldsymbol{\mathcal{G}}^{\mathrm{FV}}_{j,k+\frac{5}{2}} + \boldsymbol{\mathcal{G}}^{\mathrm{FV}}_{j,k+\frac{7}{2}}\Big].$$

The one-sided point values $\boldsymbol{U}^{\pm}_{j+\frac{1}{2},k}$ and $\boldsymbol{U}^{\pm}_{j,k+\frac{1}{2}}$ are computed using the seventh-order WENO-Z interpolation from [22].

$r = 9$ **(ninth-order schemes)**

$$(\boldsymbol{F}_{xx})_{j+\frac{1}{2},k} = \frac{1}{5040(\Delta x)^2}\Big[-9\boldsymbol{\mathcal{F}}^{\mathrm{FV}}_{j-\frac{7}{2},k} + 128\boldsymbol{\mathcal{F}}^{\mathrm{FV}}_{j-\frac{5}{2},k} - 1008\boldsymbol{\mathcal{F}}^{\mathrm{FV}}_{j-\frac{3}{2},k} + 8064\boldsymbol{\mathcal{F}}^{\mathrm{FV}}_{j-\frac{1}{2},k}$$
$$- 14350\boldsymbol{\mathcal{F}}^{\mathrm{FV}}_{j+\frac{1}{2},k} + 8064\boldsymbol{\mathcal{F}}^{\mathrm{FV}}_{j+\frac{3}{2},k} - 1008\boldsymbol{\mathcal{F}}^{\mathrm{FV}}_{j+\frac{5}{2},k} + 128\boldsymbol{\mathcal{F}}^{\mathrm{FV}}_{j+\frac{7}{2},k} - 9\boldsymbol{\mathcal{F}}^{\mathrm{FV}}_{j+\frac{9}{2},k}\Big],$$

$$(\boldsymbol{F}_{xxxx})_{j+\frac{1}{2},k} = \frac{1}{240(\Delta x)^4}\Big[7\boldsymbol{\mathcal{F}}^{\mathrm{FV}}_{j-\frac{7}{2},k} - 96\boldsymbol{\mathcal{F}}^{\mathrm{FV}}_{j-\frac{5}{2},k} + 676\boldsymbol{\mathcal{F}}^{\mathrm{FV}}_{j-\frac{3}{2},k} - 1952\boldsymbol{\mathcal{F}}^{\mathrm{FV}}_{j-\frac{1}{2},k}$$
$$+ 2730\boldsymbol{\mathcal{F}}^{\mathrm{FV}}_{j+\frac{1}{2},k} - 1952\boldsymbol{\mathcal{F}}^{\mathrm{FV}}_{j+\frac{3}{2},k} + 676\boldsymbol{\mathcal{F}}^{\mathrm{FV}}_{j+\frac{5}{2},k} - 96\boldsymbol{\mathcal{F}}^{\mathrm{FV}}_{j+\frac{7}{2},k} + 7\boldsymbol{\mathcal{F}}^{\mathrm{FV}}_{j+\frac{9}{2},k}\Big],$$

$$(\boldsymbol{F}_{xxxxxx})_{j+\frac{1}{2},k} = \frac{1}{4(\Delta x)^6}\Big[-\boldsymbol{\mathcal{F}}^{\mathrm{FV}}_{j-\frac{7}{2},k} + 12\boldsymbol{\mathcal{F}}^{\mathrm{FV}}_{j-\frac{5}{2},k} - 52\boldsymbol{\mathcal{F}}^{\mathrm{FV}}_{j-\frac{3}{2},k} + 116\boldsymbol{\mathcal{F}}^{\mathrm{FV}}_{j-\frac{1}{2},k}$$
$$- 150\boldsymbol{\mathcal{F}}^{\mathrm{FV}}_{j+\frac{1}{2},k} + 116\boldsymbol{\mathcal{F}}^{\mathrm{FV}}_{j+\frac{3}{2},k} - 52\boldsymbol{\mathcal{F}}^{\mathrm{FV}}_{j+\frac{5}{2},k} + 12\boldsymbol{\mathcal{F}}^{\mathrm{FV}}_{j+\frac{7}{2},k} - \boldsymbol{\mathcal{F}}^{\mathrm{FV}}_{j+\frac{9}{2},k}\Big],$$

$$(\boldsymbol{F}_{xxxxxxxx})_{j+\frac{1}{2},k} = \frac{1}{(\Delta x)^8}\Big[\boldsymbol{\mathcal{F}}^{\mathrm{FV}}_{j-\frac{7}{2},k} - 8\boldsymbol{\mathcal{F}}^{\mathrm{FV}}_{j-\frac{5}{2},k} + 28\boldsymbol{\mathcal{F}}^{\mathrm{FV}}_{j-\frac{3}{2},k} - 56\boldsymbol{\mathcal{F}}^{\mathrm{FV}}_{j-\frac{1}{2},k}$$
$$+ 70\boldsymbol{\mathcal{F}}^{\mathrm{FV}}_{j+\frac{1}{2},k} - 56\boldsymbol{\mathcal{F}}^{\mathrm{FV}}_{j+\frac{3}{2},k} + 28\boldsymbol{\mathcal{F}}^{\mathrm{FV}}_{j+\frac{5}{2},k} - 8\boldsymbol{\mathcal{F}}^{\mathrm{FV}}_{j+\frac{7}{2},k} + \boldsymbol{\mathcal{F}}^{\mathrm{FV}}_{j+\frac{9}{2},k}\Big],$$

$$(\boldsymbol{G}_{yy})_{j,k+\frac{1}{2}} = \frac{1}{5040(\Delta y)^2}\Big[-9\boldsymbol{\mathcal{G}}^{\mathrm{FV}}_{j,k-\frac{7}{2}} + 128\boldsymbol{\mathcal{G}}^{\mathrm{FV}}_{j,k-\frac{5}{2}} - 1008\boldsymbol{\mathcal{G}}^{\mathrm{FV}}_{j,k-\frac{3}{2}} + 8064\boldsymbol{\mathcal{G}}^{\mathrm{FV}}_{j,k-\frac{1}{2}}$$
$$- 14350\boldsymbol{\mathcal{G}}^{\mathrm{FV}}_{j,k+\frac{1}{2}} + 8064\boldsymbol{\mathcal{G}}^{\mathrm{FV}}_{j,k+\frac{3}{2}} - 1008\boldsymbol{\mathcal{G}}^{\mathrm{FV}}_{j,k+\frac{5}{2}} + 128\boldsymbol{\mathcal{G}}^{\mathrm{FV}}_{j,k+\frac{7}{2}} - 9\boldsymbol{\mathcal{G}}^{\mathrm{FV}}_{j,k+\frac{9}{2}}\Big],$$

$$(\boldsymbol{G}_{yyyy})_{j,k+\frac{1}{2}} = \frac{1}{240(\Delta y)^4}\Big[7\boldsymbol{\mathcal{G}}^{\mathrm{FV}}_{j,k-\frac{7}{2}} - 96\boldsymbol{\mathcal{G}}^{\mathrm{FV}}_{j,k-\frac{5}{2}} + 676\boldsymbol{\mathcal{G}}^{\mathrm{FV}}_{j,k-\frac{3}{2}} - 1952\boldsymbol{\mathcal{G}}^{\mathrm{FV}}_{j,k-\frac{1}{2}}$$
$$+ 2730\boldsymbol{\mathcal{G}}^{\mathrm{FV}}_{j,k+\frac{1}{2}} - 1952\boldsymbol{\mathcal{G}}^{\mathrm{FV}}_{j,k+\frac{3}{2}} + 676\boldsymbol{\mathcal{G}}^{\mathrm{FV}}_{j,k+\frac{5}{2}} - 96\boldsymbol{\mathcal{G}}^{\mathrm{FV}}_{j,k+\frac{7}{2}} + 7\boldsymbol{\mathcal{G}}^{\mathrm{FV}}_{j,k+\frac{9}{2}}\Big],$$

$$(\boldsymbol{G}_{yyyyyy})_{j,k+\frac{1}{2}} = \frac{1}{4(\Delta y)^6}\Big[-\boldsymbol{\mathcal{G}}^{\mathrm{FV}}_{j,k-\frac{7}{2}} + 12\boldsymbol{\mathcal{G}}^{\mathrm{FV}}_{j,k-\frac{5}{2}} - 52\boldsymbol{\mathcal{G}}^{\mathrm{FV}}_{j,k-\frac{3}{2}} + 116\boldsymbol{\mathcal{G}}^{\mathrm{FV}}_{j,k-\frac{1}{2}}$$
$$- 150\boldsymbol{\mathcal{G}}^{\mathrm{FV}}_{j,k+\frac{1}{2}} + 116\boldsymbol{\mathcal{G}}^{\mathrm{FV}}_{j,k+\frac{3}{2}} - 52\boldsymbol{\mathcal{G}}^{\mathrm{FV}}_{j,k+\frac{5}{2}} + 12\boldsymbol{\mathcal{G}}^{\mathrm{FV}}_{j,k+\frac{7}{2}} - \boldsymbol{\mathcal{G}}^{\mathrm{FV}}_{j,k+\frac{9}{2}}\Big],$$

$$(\boldsymbol{G}_{yyyyyyyy})_{j,k+\frac{1}{2}} = \frac{1}{(\Delta y)^8}\Big[\boldsymbol{\mathcal{G}}^{\mathrm{FV}}_{j,k-\frac{7}{2}} - 8\boldsymbol{\mathcal{G}}^{\mathrm{FV}}_{j,k-\frac{5}{2}} + 28\boldsymbol{\mathcal{G}}^{\mathrm{FV}}_{j,k-\frac{3}{2}} - 56\boldsymbol{\mathcal{G}}^{\mathrm{FV}}_{j,k-\frac{1}{2}}$$
$$+ 70\boldsymbol{\mathcal{G}}^{\mathrm{FV}}_{j,k+\frac{1}{2}} - 56\boldsymbol{\mathcal{G}}^{\mathrm{FV}}_{j,k+\frac{3}{2}} + 28\boldsymbol{\mathcal{G}}^{\mathrm{FV}}_{j,k+\frac{5}{2}} - 8\boldsymbol{\mathcal{G}}^{\mathrm{FV}}_{j,k+\frac{7}{2}} + \boldsymbol{\mathcal{G}}^{\mathrm{FV}}_{j,k+\frac{9}{2}}\Big].$$

The one-sided point values $\boldsymbol{U}^{\pm}_{j+\frac{1}{2},k}$ and $\boldsymbol{U}^{\pm}_{j,k+\frac{1}{2}}$ are computed using the ninth-order WENO-Z interpolation from [22].

4 Numerical Results

In this section, we present the numerical simulations conducted using the schemes described in §3 for three 2-D Riemann problems and the KH instability problem.

In all of the examples, we take a uniform mesh with $\Delta x = \Delta y = 1/1024$ on the computational domain $[0,1] \times [0,1]$. We numerically integrate the ODE systems (3.4) and (3.8) using the three-stage third-order strong stability preserving Runge-Kutta method (see, e.g., [23,24]) and use the CFL number 0.45 for the schemes employing the LCDCU and LDCU numerical fluxes and 0.1, when the VFV numerical fluxes are utilized.

Below, we will use the following notation for the solutions computed using the same numerical flux, but with different orders of the resulting scheme: $(\rho_\ell, \boldsymbol{m}_\ell, S_\ell)$, $\ell(r) = 1, \ldots, 6$ are solutions computed by the first-, second-, third-, fifth-, seventh-, and ninth-order schemes, respectively, that is, $\ell(1) = 1$, $\ell(2) = 2$, $\ell(3) = 3$, $\ell(5) = 4$, $\ell(7) = 5$, and $\ell(9) = 6$. In accordance with the concept of $\mathcal{K}$-convergence described in Theorem 2.5, we will average these solutions to obtain $(\widetilde{\rho}_n, \widetilde{\boldsymbol{m}}_n, \widetilde{S}_n)^\top :=$ $\frac{1}{n} \sum_{\ell=1}^{n} (\rho_\ell, \boldsymbol{m}_\ell, S_\ell)^\top$, where $n = 1, \ldots, 6$.

In some of the examples below, oscillatory solutions are to be captured. As explained in Remark 2.1, such solutions should be represented as a Young measure in the phase space. In fact, when the solution is a weak solution, the corresponding Young measure is expected to be a Dirac δ-function. In order to check whether the obtained solution is a genuine DW solution or a weak solution in the sense of distributions, we will approximate the probability density function (PDF) of the Young measure $\{\mathcal{V}_{x,y,t}\}$ as follows.

We take a certain small rectangular subdomain $\widetilde{\Omega}$ and compute

$$\underline{\rho} := \min_{(x_j,y_k) \in \widetilde{\Omega}} \rho_{j,k} \quad \text{and} \quad \overline{\rho} := \max_{(x_j,y_k) \in \widetilde{\Omega}} \rho_{j,k}.$$

We then introduce $\Delta\rho := (\overline{\rho} - \underline{\rho})/30$ and the following partition of the interval $[\underline{\rho}, \overline{\rho}]$:

$$[\underline{\rho}, \overline{\rho}] = \bigcup_{i=1}^{30} \left[\rho^{(i-\frac{1}{2})}, \rho^{(i+\frac{1}{2})} \right), \quad \text{where} \quad \rho^{(\frac{1}{2})} = \underline{\rho}, \quad \rho^{(i+\frac{1}{2})} = \rho^{(i-\frac{1}{2})} + \Delta\rho, \quad i = 2, \ldots, 30.$$

The distribution of the dataset formed by the values $\rho_{j,k}$ across all $C_{j,k} \subseteq \widetilde{\Omega}$ is represented by a function $\sigma_\ell = \sigma_\ell(\rho)$, where the subscript $\ell = \ell(r)$ indicates that the density values have been computed using the r-th order scheme. More specifically, $\sigma_\ell(\rho^{(i)})$ denotes the number of cells $C_{j,k}$ for which the computed values $\rho_{j,k}$ fall within the interval $\left[\rho^{(i-\frac{1}{2})}, \rho^{(i+\frac{1}{2})} \right)$. Additionally, we apply a normalization such that

$$\Delta\rho \sum_{i=1}^{30} \sigma_\ell(\rho^{(i)}) = 1.$$

In order to obtain a strong convergence, we average the sequence $\{\sigma_\ell\}$ and introduce $\widetilde{\sigma}_n := \frac{1}{n} \sum_{\ell=1}^{n} \sigma_\ell$, $n = 1, \ldots, 6$.

4.1   2-D Riemann Problems

We begin by considering three 2-D Riemann problems from [26] (see also [34,35,38]): Configurations 2–4. The details on the initial data, subject to the free boundary conditions, are specified below.

Configuration 2.   In the first example, the initial data are

$$(\rho, u, v, p)(x, y, 0) = \begin{cases} (1, 0, 0, 1), & x > 0.5, \ y > 0.5, \\ (0.5197, -0.7259, 0, 0.4), & x < 0.5, \ y > 0.5, \\ (1, -0.7259, -0.7259, 1), & x < 0.5, \ y < 0.5, \\ (0.5197, 0, -0.7259, 0.4), & x > 0.5, \ y < 0.5, \end{cases}$$

and far from the center of the computational domain, the solution consists of four rarefaction waves.

We compute the numerical solutions until the final time $T = 0.2$ using the studied schemes and show the results, obtained by the first-, third-, and ninth-order schemes in Figure 4.1. As one can

see, the use of all three numerical fluxes leads to similar solutions, especially when the ninth-order results are compared. The absence of oscillations in the obtained numerical solutions indicates that they converge to the same weak solution.
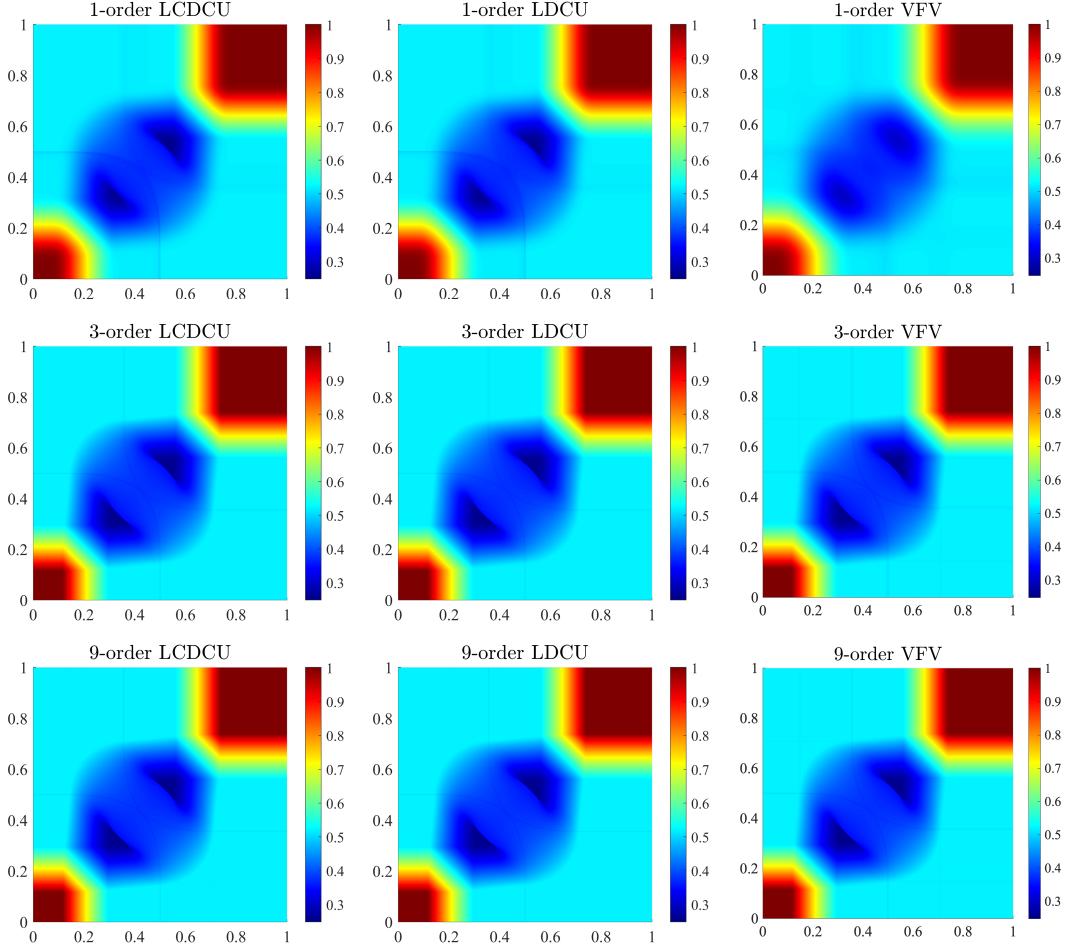

Figure 4.1: Configuration 2: Density computed by the first- (top row), third- (middle row), and ninth-order (bottom row) LCDCU (left column), LDCU (middle column), and VFV (right column) schemes.

Configuration 4. In this example, the initial data are

$$(\rho, u, v, p)(x, y, 0) = \begin{cases} (1.1, 0, 0, 1.1), & x > 0.5, \ y > 0.5, \\ (0.5065, 0.8939, 0, 0.35), & x < 0.5, \ y > 0.5, \\ (1.1, 0.8939, 0.8939, 1.1), & x < 0.5, \ y < 0.5, \\ (0.5065, 0, 0.8939, 0.35), & x > 0.5, \ y < 0.5, \end{cases}$$

and far from the center of the computational domain, the solution consists of four shock waves.

We compute the numerical solutions until the final time $T = 0.25$ using the studied schemes and show the results, obtained by the first-, third-, and ninth-order schemes in Figure 4.2. Although the solutions are not smooth, the results exhibit clear similarities, indicating that the different methods converge to the same weak solution.
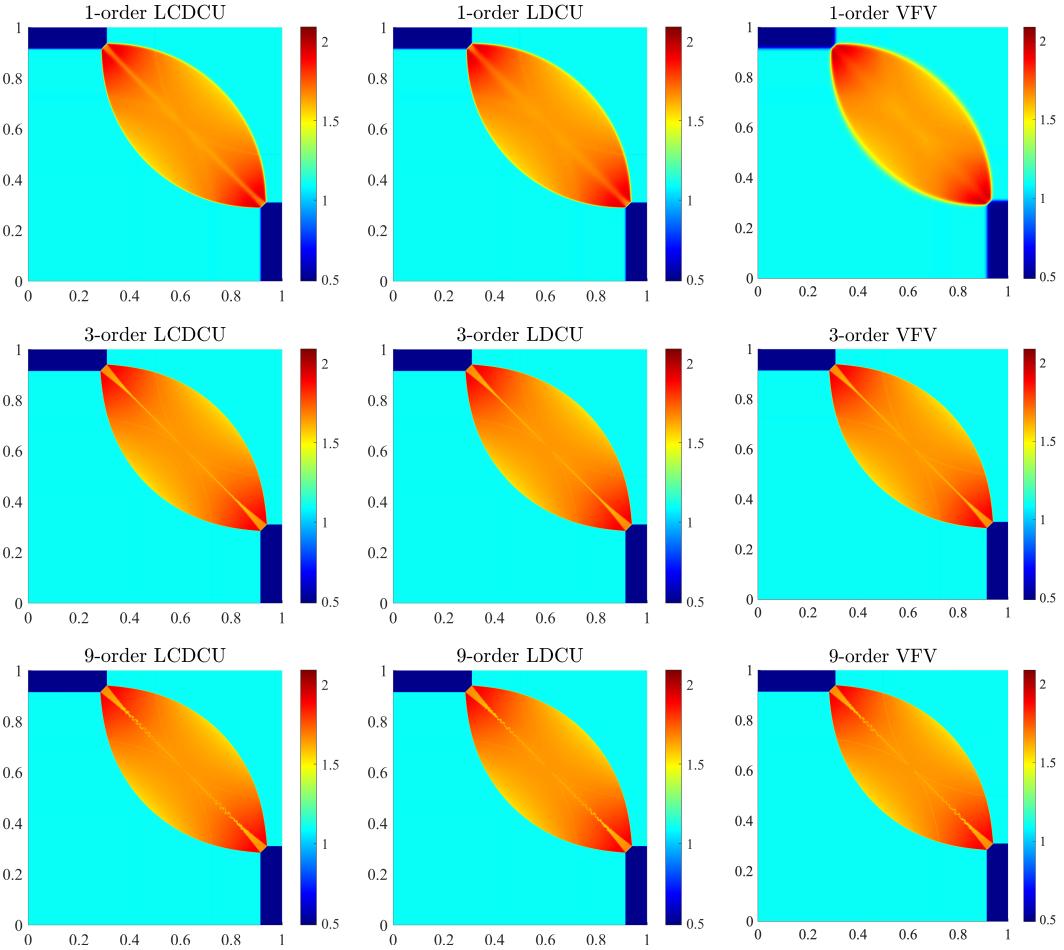
Figure 4.2: Configuration 4: Density computed by the first- (top row), third- (middle row), and ninth-order (bottom row) LCDCU (left column), LDCU (middle column), and VFV (right column) schemes.

Configuration 3. In this example, the initial data are

$$
(\rho, u, v, p)(x, y, 0) = \begin{cases}
(1.5, 0, 0, 1.5), & x > 0.8, \ y > 0.8, \\
(0.5323, 1.206, 0, 0.3), & x < 0.8, \ y > 0.8, \\
(0.138, 1.206, 1.206, 0.029), & x < 0.8, \ y < 0.8, \\
(0.5323, 0, 1.206, 0.3), & x > 0.8, \ y < 0.8,
\end{cases}
$$

and far from the center of the computational domain, the solution consists of four shock waves.

We compute the numerical solutions until the final time $T = 0.8$ using the studied schemes and show the results, obtained by the first-, third-, and seventh-order schemes in Figure 4.3. As one can see, the higher-order schemes can better capture the sideband instability of the jet in the zones of strong along-jet velocity shear and the instability along the jet's neck. This indicates that the numerical methods may produce true DW solutions, with convergence being only weak, as indicated by Theorem 2.2. We then investigate the convergence behavior of the average quantities. In Figure 4.4, we present the average densities $\widetilde{\rho}_3$, $\widetilde{\rho}_4$, and $\widetilde{\rho}_5$ for the three studied methods. It can be observed that the average densities exhibit similar profiles across the different orders of accuracy, indicating a strong convergence of the averaged sequence. Note, however, that the limiting DW solution for different methods may differ; see the discussion below.

Next, we approximate the time averages of a DW solution by evaluating the time averages of the
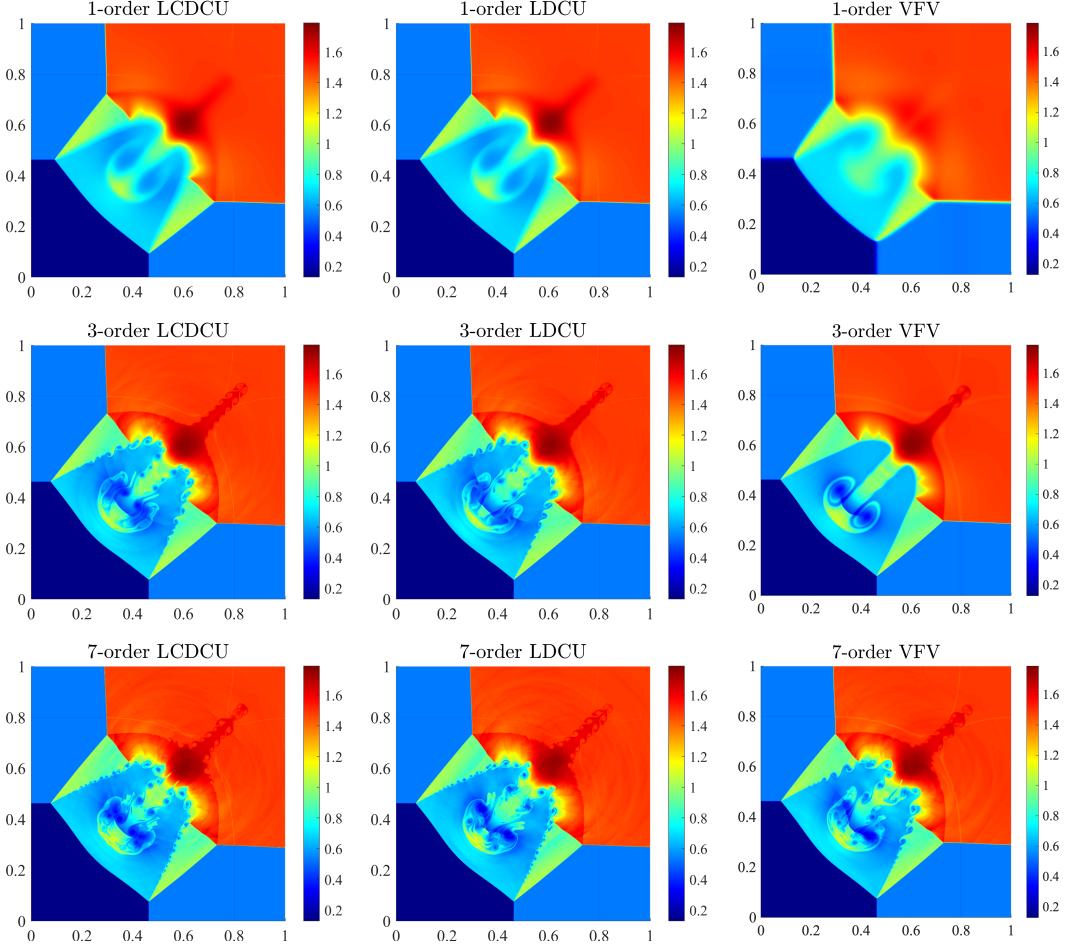
Figure 4.3: Configuration 3: Density computed by the first- (top row), third- (middle row), and seventh-order (bottom row) LCDCU (left column), LDCU (middle column), and VFV (right column) schemes.

computed densities, which are denoted by

$$\rho_\ell^T := \frac{1}{T} \int_0^T \rho_\ell(\cdot, t)\, \mathrm{d}t,$$

where T is the final time. Figure 4.5 shows ρ_ℓ^T for the three studied methods and Figure 4.6 presents the time averages of $\widetilde{\rho}_5$, which we denote by

$$\widetilde{\rho}_5^T := \frac{1}{T} \int_0^T \widetilde{\rho}_5(\cdot, t)\, \mathrm{d}t.$$

These figures suggest that there is almost no difference between the time averaged flows computed by different methods. We note that time averages $\widetilde{\rho}_5^T$ are typically used in the analysis of turbulent flows.

Finally, we establish the experimental PDFs of the Young measures for the three studied schemes. In this example, we choose the following two subdomains:

$$\widetilde{\Omega}_1 = [0.42, 0.43] \times [0.63, 0.64] \quad \text{and} \quad \widetilde{\Omega}_2 = [0.60, 0.61] \times [0.37, 0.38],$$

compute $\widetilde{\sigma}_3$, $\widetilde{\sigma}_4$, and $\widetilde{\sigma}_5$, and plot the obtained results in Figure 4.7. As one can see, the average sequences from various numerical methods yield different limiting PDFs, particularly for subdomain $\widetilde{\Omega}_1$, indicating that the order-averaged solutions converge to different DW solutions.
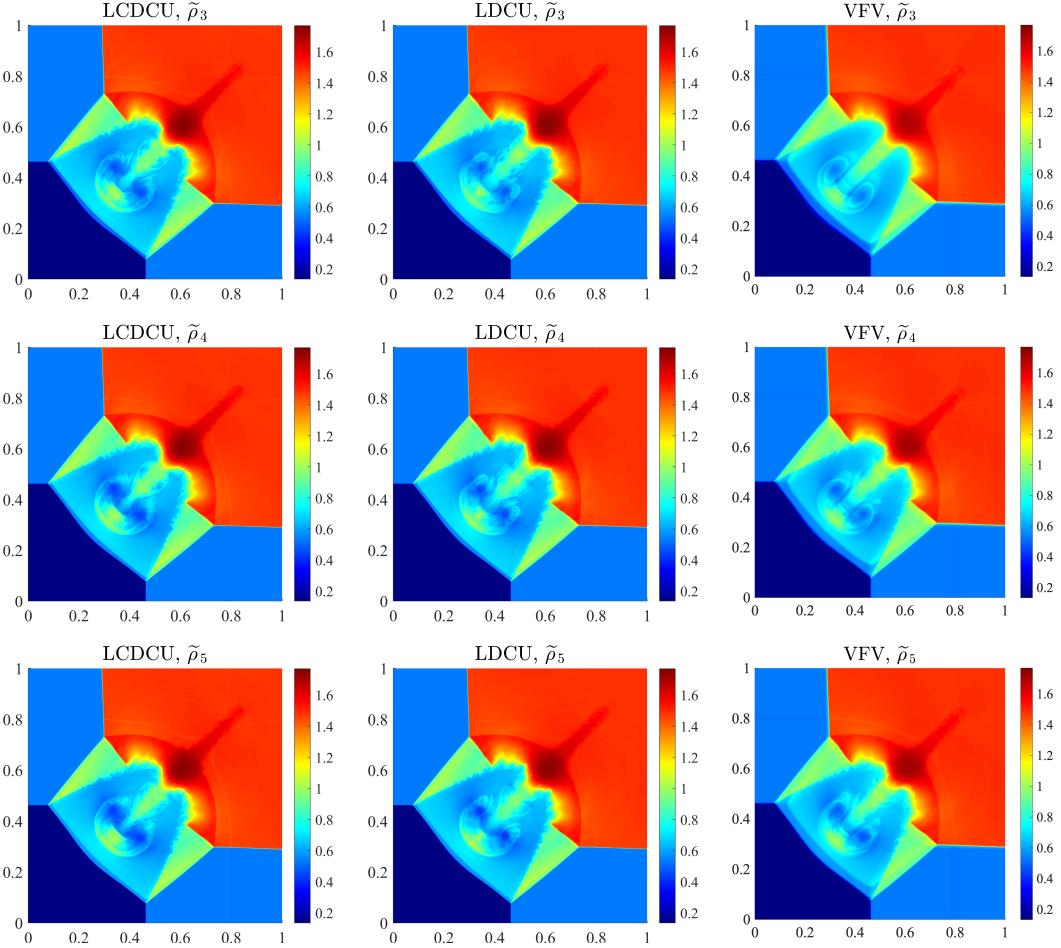
Figure 4.4: Configuration 3: $\widetilde{\rho}_3$ (top row), $\widetilde{\rho}_4$ (middle row), and $\widetilde{\rho}_5$ (bottom row) computed by the LCDCU (left column), LDCU (middle column), and VFV (right column) schemes.

4.2 Kelvin-Helmholtz (KH) Instability

In the last example, we consider the KH instability problem taken from [16] with the following initial conditions:

$$(\rho, u, v, p)(x, y, 0) = \begin{cases} (2, -0.5, 0, 2.5), & \text{if } 0.25 + 0.01Y_1(x, \omega) < y < 0.75 + 0.01Y_2(x, \omega), \\ (1, 0.5, 0, 2.5), & \text{otherwise}, \end{cases}$$

where

$$Y_j(x, \omega) = \sum_{n=1}^{10} a_j^n(\omega) \cos\left(b_j^n(\omega) + 2n\pi x\right), \quad j = 1, 2,$$

with $a_j^n = a_j^n(\omega) \in [0, 1]$ and $b_j^n = b_j^n(\omega) \in (-\pi, \pi)$ being fixed random numbers, and a_j^n being normalized such that $\sum_{n=1}^{10} a_j^n = 1$. The particular values of a_j^n and b_j^n, which have been generated by `rand` in MATLAB, are given in Table 4.1. The boundary conditions in this example are periodic.

We compute the numerical solutions until the final time $T = 2$ using the studied schemes and show the results, obtained by the first-, third-, and ninth-order schemes in Figure 4.8. The results indicate that the flow is unstable, with an increasing number of vortices generated when higher-order schemes are employed. Additionally, it is evident that different schemes converge to different DW solutions. This suggests that the numerical solutions will not strongly converge as the order of accuracy increases.

We then consider the $\mathcal{K}$-convergence of the numerical solutions over different orders. In Figure 4.9, we present $\widetilde{\rho}_3$, $\widetilde{\rho}_4$, $\widetilde{\rho}_5$, and $\widetilde{\rho}_6$, where one can see that, in contrast to Figure 4.8, the average
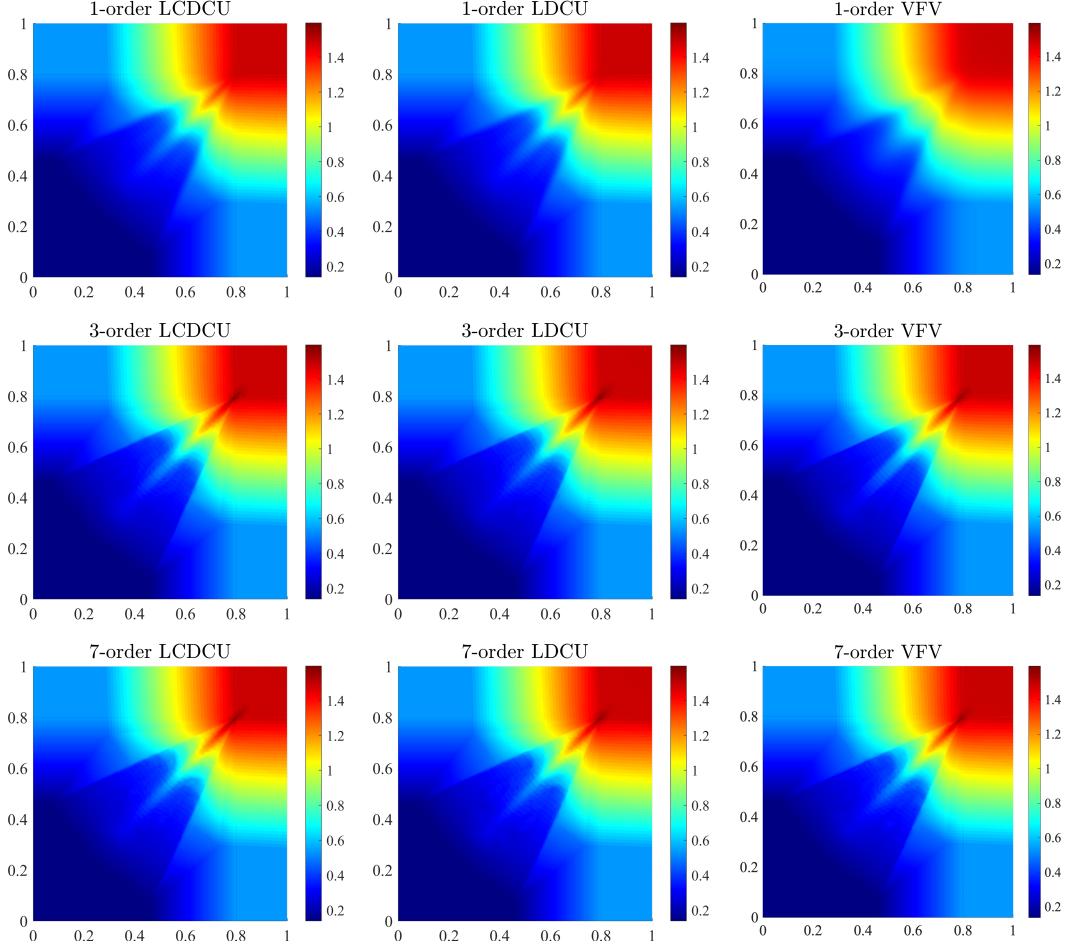
Figure 4.5: Configuration 3: ρ_1^T (top row), ρ_3^T (middle row), and ρ_5^T (bottom row) computed by the LCDCU (left column), LDCU (middle column), and VFV (right column) schemes.
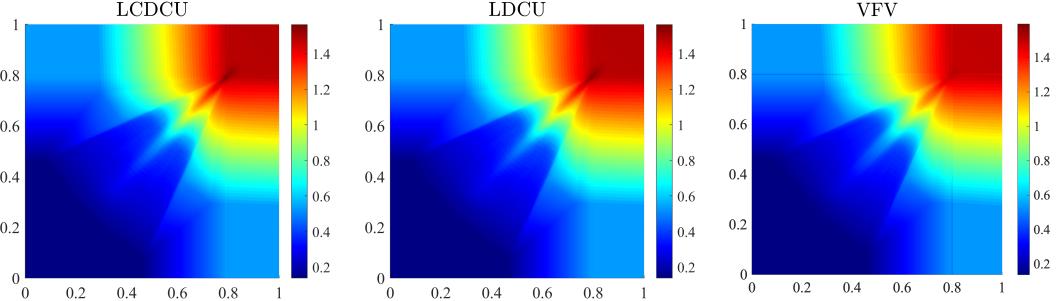
Figure 4.6: Configuration 3: $\widetilde{\rho}_5^T$ computed by the LCDCU (left), LDCU (middle), and VFV (right) schemes.

density profiles show similarities for different n, suggesting that the sequence of averages is convergent. Additionally, we observe that for different methods, the limits of the average density differ significantly. This indicates that the numerical approximations generated by different methods converge to different DW solutions.

Next, we consider the difference between the time averages of the numerical solutions. Figure 4.10 presents the time averages of the density computed by the three methods. Similarly, we can observe that they are convergent as the order increases. In addition, the difference between the limiting average densities is pronounced. In Figure 4.11, we show the time averages of the mean density for the three methods. Remarkably, they look very similar. This phenomenon suggests that there is some consistency in the measure-valued solutions produced by different numerical methods.
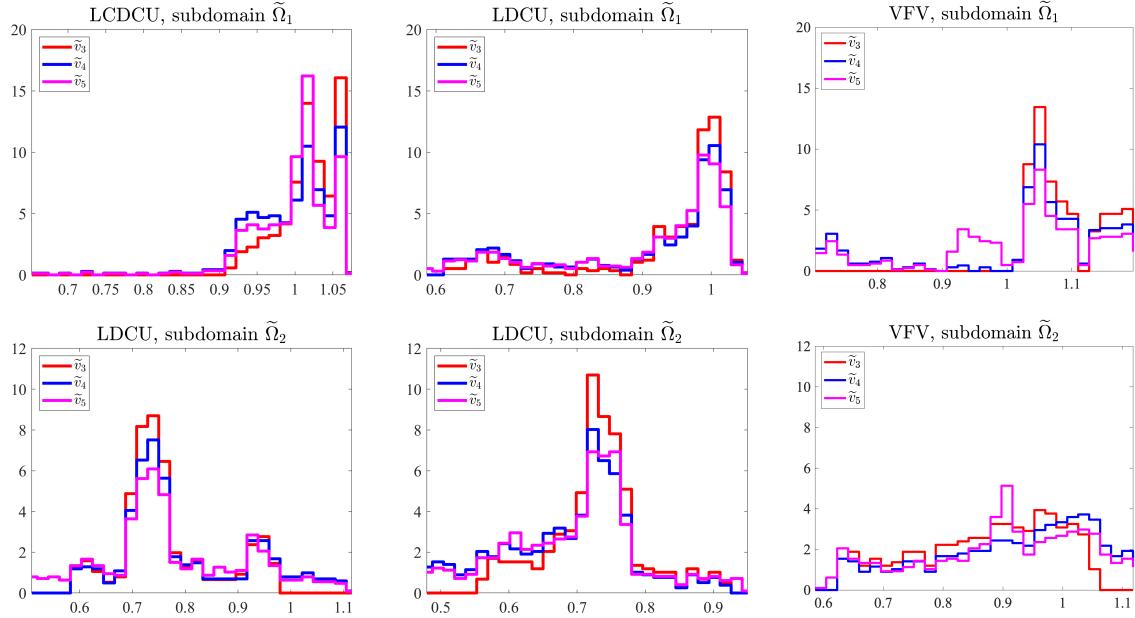
Figure 4.7: Configuration 3: $\widetilde{\sigma}_3$, $\widetilde{\sigma}_4$, and $\widetilde{\sigma}_5$ computed by the LCDCU (left column), LDCU (middle column), and VFV (right column) schemes in the subdomains $\widetilde{\Omega}_1$ (top row) and $\widetilde{\Omega}_2$ (bottom row).

	a_1^n	a_2^n	b_1^n	b_2^n
1	6.848086824246653e-08	9.373025805955863e-03	-0.973625473853271	3.10750325239443
2	4.450348128947341e-03	1.976861219341060e-02	2.33221742979395	1.74829850637860
3	6.156955958786613e-02	1.29928159795144e-01	-2.57661895600041	-3.01803367486339
4	1.16481555805349e-01	2.15403817045303e-01	2.43965931651801	-2.07430785001108
5	1.68204784555961e-01	1.758678905771403e-02	1.26278768686501	3.10856394704146
6	1.46413246162863e-01	2.11994809652299e-01	1.47373734867445	1.59399689987015
7	5.857224323849688e-02	2.134903127162342e-02	-1.25553236484458	-1.77202310331374
8	1.59868678328304e-01	1.48283301108284e-01	-2.82920698380582	1.00086476379714
9	1.39003488203723e-01	1.98161392506709e-01	2.56472949845762	0.245159802027399
10	1.45436027507622e-01	2.815106156355688e-02	-2.52798558841484	-0.125265541490568

Table 4.1: The values of a_1^n, a_2^n, b_1^n, and b_2^n for $n = 1, \ldots, 10$ generated by `rand` in MATLAB.

To illustrate the differences in numerical results, we compare the approximate PDFs of the Young measures. We select two subdomains:

$$\widetilde{\Omega}_1 = [0.50, 0.51] \times [0.25, 0.26] \quad \text{and} \quad \widetilde{\Omega}_2 = [0.15, 0.16] \times [0.75, 0.76],$$

and present the obtained results in Figure 4.12. It is evident that these PDFs differ significantly, particularly between those computed by the VFV method and by the other two methods. This indicates that the different methods can yield different DW solutions.

4.3 Convergence of Averages over Orders

In this section, we evaluate the convergence of the averages over orders of accuracy. We estimate the errors of these averages using the quantities

$$\|\widetilde{\rho}_n - \widetilde{\rho}_6\|_{L_1(\Omega)}, \quad n = 1, \ldots, 5,$$
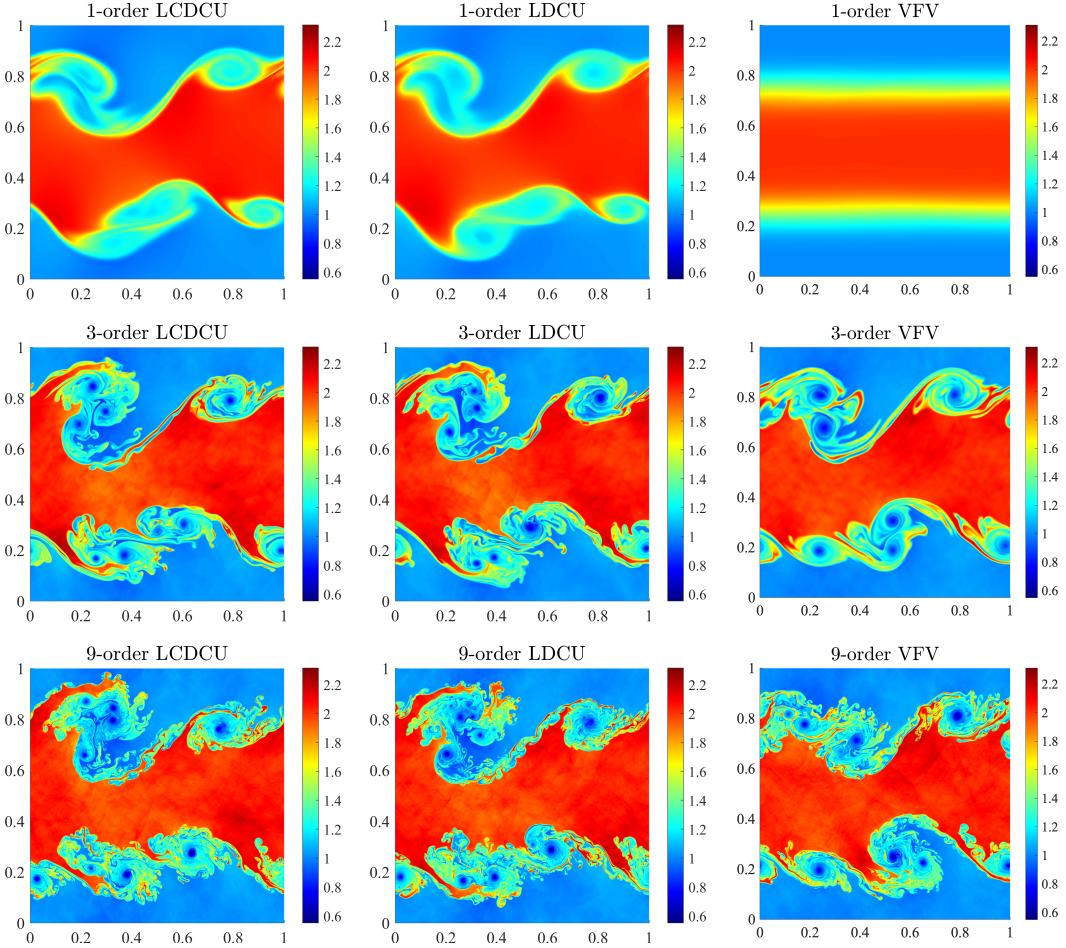
Figure 4.8: KH Instability: Density computed by the first- (top row), third- (middle), and ninth-order (bottom row) LCDCU (left column), LDCU (middle column), and VFV (right column) schemes.

where $\widetilde{\rho}_6$ serves as a reference solution. In Figure 4.13, we present the errors associated with the two Riemann problems (Configurations 2 and 4) and KH instability problem. It is evident that the errors decrease as n increases: This behavior demonstrates the $\mathcal{K}$-convergence of the sequence of averages.

To further analyze the behavior of errors with respect to the orders, we utilize the least squares data fitting to approximate the error functions, which take the form of power functions of n; see Table 4.2. One can observe a substantial difference in the decay rates for different problems. For Configuration 2, in which the computed weak solution is continuous, the convergence is the fastest. It is somewhat slower for the Configuration 4, in which the solution is discontinuous, but still not a truly DW solution. Finally, for the KH instability problem, which admits genuine measure-valued solutions, the convergence is substantially slower and, as we can see from Figure 4.13, the magnitude of the errors is much larger than those obtained for the considered Riemann problems.

	LCDCU	LDCU	VFV
Configuration 2	$0.0043\,n^{-1.82}$	$0.0044\,n^{-1.82}$	$0.0093\,n^{-1.77}$
Configuration 4	$0.0053\,n^{-1.60}$	$0.0059\,n^{-1.63}$	$0.0136\,n^{-1.75}$
KH Instability	$0.1335\,n^{-0.98}$	$0.1104\,n^{-0.90}$	$0.1382\,n^{-1.04}$

Table 4.2: The errors of the average density as functions of n for the LCDCU, LDCU, and VFV schemes.
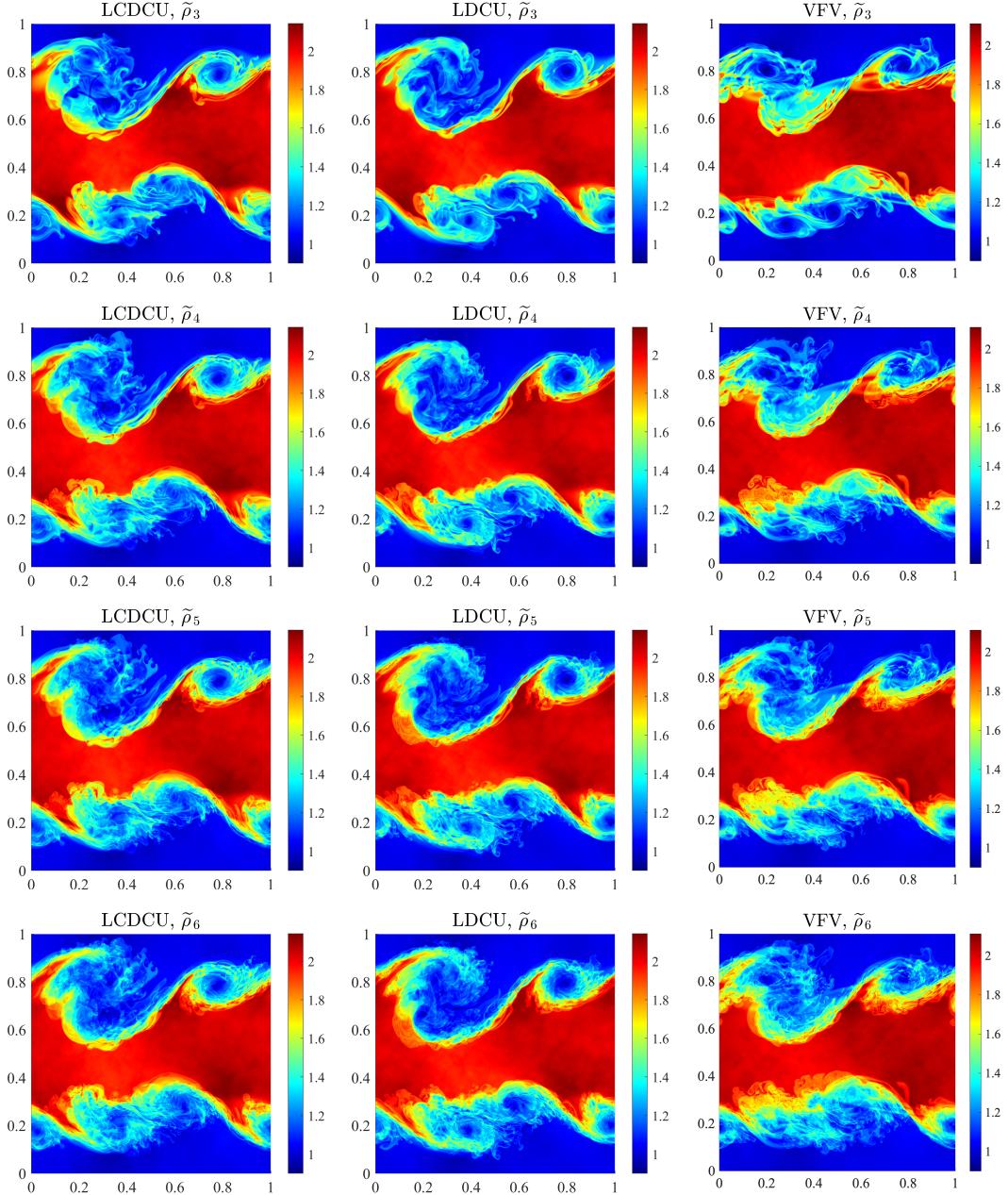
Figure 4.9: KH Instability: $\widetilde{\rho}_3$ (top row), $\widetilde{\rho}_4$ (second row), $\widetilde{\rho}_5$ (third row), and $\widetilde{\rho}_6$ (bottom row) computed by the LCDCU (left column), LDCU (middle column), and VFV (right column) schemes.

4.4   Selection Criteria

As seen in the previous results (Configuration 3 for the 2-D Riemann problem and the KH instability problem), different numerical schemes can converge to different DW solutions. Consequently, we need additional criteria to select the physically relevant one. In this section, we analyze potential selection criteria based on the entropy production and energy defects. Notice that similar selection criteria were studied theoretically in [17, 20].

We denote the integral of the average total entropy over orders up to n by

$$\mathcal{S}^n(t) := \int_\Omega \widetilde{S}_n(x, y, t) \, \mathrm{d}x\mathrm{d}y.$$
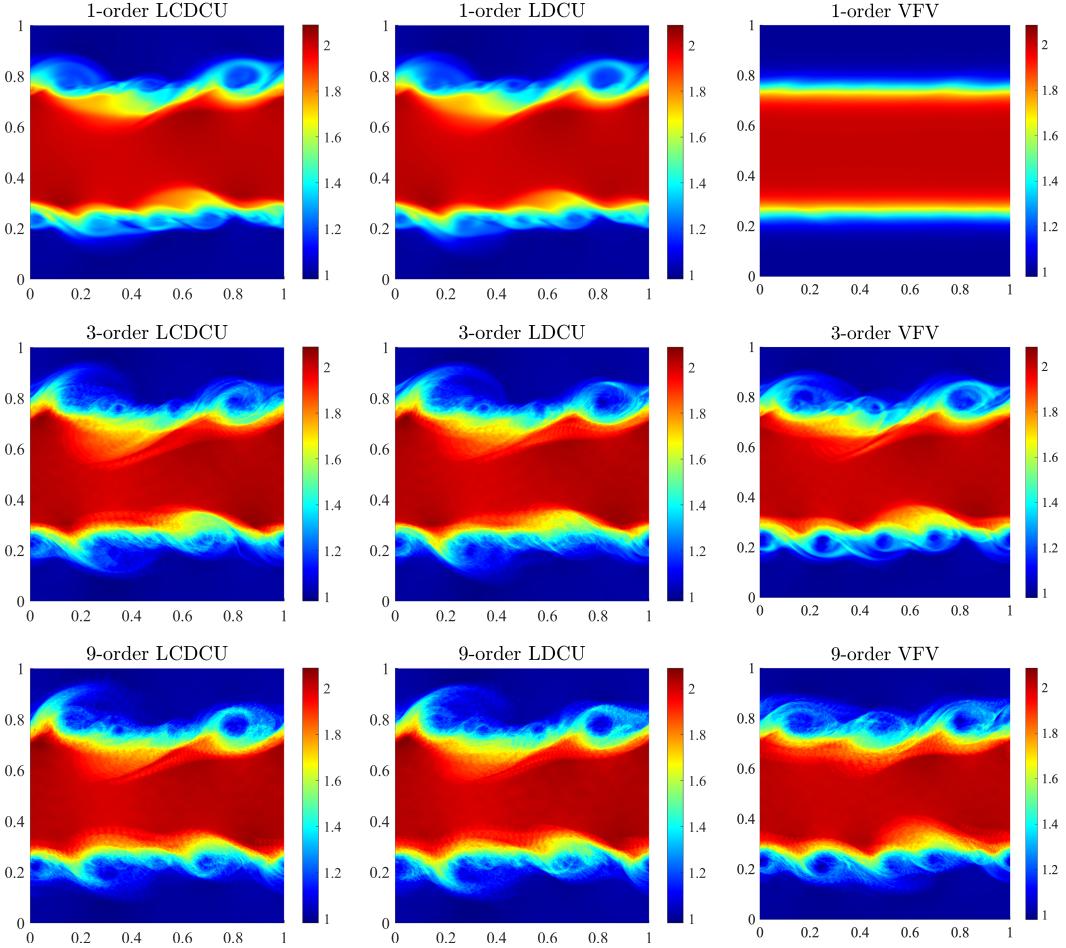
Figure 4.10: KH Instability: ρ_1^T (top row), ρ_3^T (middle row), and ρ_6^T (bottom row) computed by the LCDCU (left column), LDCU (middle column), and VFV (right column) schemes.
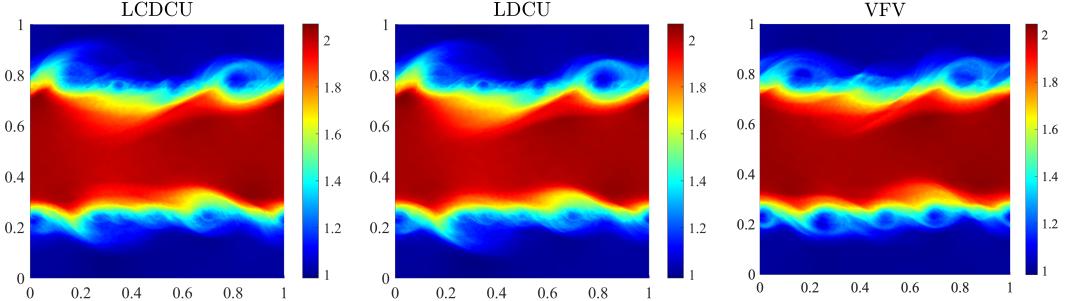
Figure 4.11: KH Instability: $\widetilde{\rho}_6^T$ computed by the LCDCU (left), LDCU (middle), and VFV (right) schemes.

The turbulent energy and total energy are defined by

$$\mathcal{E}_1^n(t) := \int_\Omega \widetilde{E}_n(x,y,t)\,\mathrm{d}x\mathrm{d}y = \int_\Omega \frac{1}{n} \sum_{\ell=1}^n \left[\frac{|\boldsymbol{m}_\ell|^2}{2\rho_\ell} + \rho_\ell e(\rho_\ell, S_\ell) \right] \mathrm{d}x\mathrm{d}y,$$

$$\mathcal{E}_2^n(t) := \int_\Omega E\big(\widetilde{\rho}_n(x,y,t), \widetilde{\boldsymbol{m}}_n(x,y,t), \widetilde{S}_n(x,y,t)\big)\mathrm{d}x\mathrm{d}y = \int_\Omega \frac{|\widetilde{\boldsymbol{m}}_n|^2}{2\widetilde{\rho}_n} + \widetilde{\rho}_n e\big(\widetilde{\rho}_n, \widetilde{S}_n\big)\mathrm{d}x\mathrm{d}y,$$

respectively, and the energy defect is defined by

$$\mathcal{D}_{\mathrm{E}}^n(t) := \int_\Omega \left| \widetilde{E}_n(x,y,t) - E\big(\widetilde{\rho}_n(x,y,t), \widetilde{\boldsymbol{m}}_n(x,y,t), \widetilde{S}_n(x,y,t)\big) \right| \mathrm{d}x\mathrm{d}y.$$
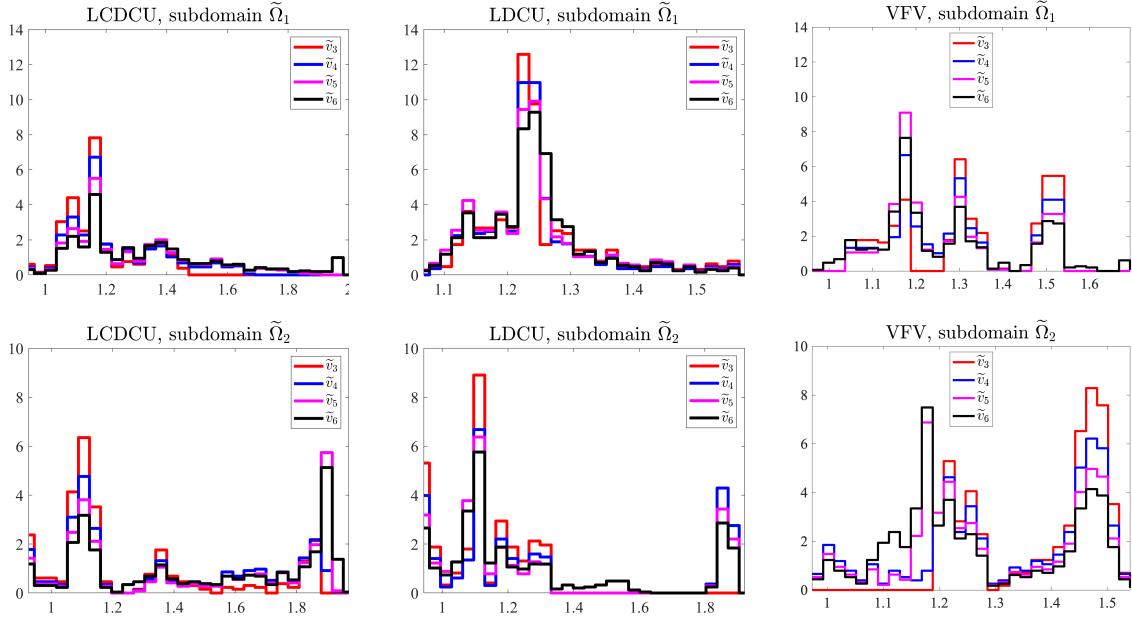
Figure 4.12: KH Instability: $\widetilde{\sigma}_3$, $\widetilde{\sigma}_4$, $\widetilde{\sigma}_5$, and $\widetilde{\sigma}_6$ computed by the LCDCU (left column), LDCU (middle column), and VFV (right column) schemes in the subdomains $\widetilde{\Omega}_1$ (top row) and $\widetilde{\Omega}_2$ (bottom row).
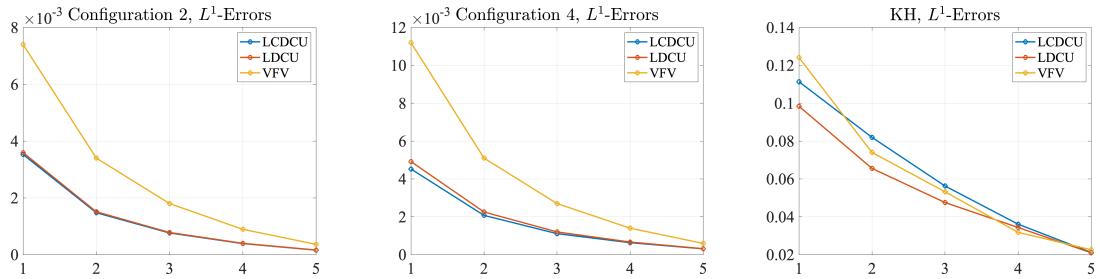
Figure 4.13: The L_1-errors of the average density computed by the studied schemes for Configuration 2 (left), Configuration 4 (middle), and KH instability (right) problems.

Possible selection criteria for DW solutions are (i) the maximization of entropy production, (ii) the minimization of energy defect, and (iii) the maximization of energy defect. We stress that criteria (ii) and (iii) are not contradictory since they help select the solutions with either the minimal or maximal oscillatory (turbulent) structures, respectively. Based on the numerical solutions obtained by different methods, we compare their respective entropy production and energy defects.

We begin with Configuration 3 for the 2-D Riemann problem. The time evolution of the total entropy $\mathcal{S}^5$ and energy defects $\mathcal{D}_{\mathrm{E}}^5$ are shown in Figure 4.14, and their time averages are presented in Table 4.3. As expected, the oscillations in specific regions of the flow, observed in §4.1, lead to energy defects. It can be observed that the LCDCU and LDCU schemes produce smaller defects compared to the VFV schemes. At the same time, these two methods result in smaller entropy productions. Consequently, selection criteria (i) and (iii) prioritize the VFV schemes, while criterion (ii) prioritizes the LCDCU schemes. We also emphasize that since the computed solutions develop oscillatory structures in a small part of the computational domain only, the magnitude of the energy defects is quite small in this example.

Finally, we focus on the total entropy $\mathcal{S}^6$ and the energy defect $\mathcal{D}_{\mathrm{E}}^6$ for the KH instability problem. The time evolutions and time averages of these quantities are shown in Figure 4.15 and Table 4.4, respectively. The magnitude of energy defects is substantially larger than in the Configuration 3 example, indicating that the limiting DW solutions are clearly not weak solutions in the sense of distributions. This observation is consistent with the figures of the averaged numerical solutions presented in §4.3. This suggests that selection criterion (iii) is a physically relevant one in this
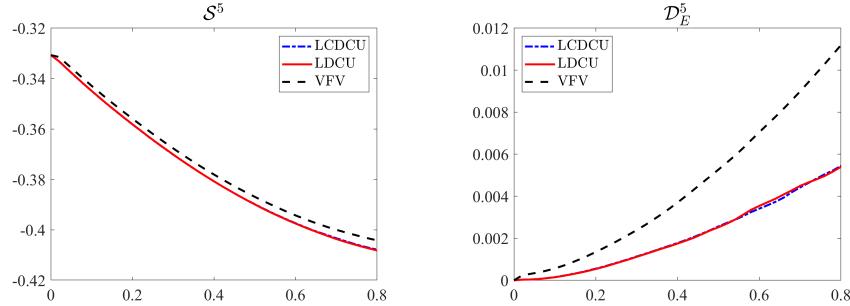
Figure 4.14: Configuration 3: Time evolution of the average entropy $\mathcal{S}^5$ (left) and energy defects $\mathcal{D}_{\mathrm{E}}^5$ (right) computed by the LCDCU, LDCU, and VFV schemes.

	LCDCU	LDCU	VFV
$\frac{1}{T}\int_0^T \mathcal{S}^5(t)\,\mathrm{d}t$	-0.3778	-0.3778	-0.3741
$\frac{1}{T}\int_0^T \mathcal{E}_1^5(t)\,\mathrm{d}t$	1.3690	1.3690	1.3541
$\frac{1}{T}\int_0^T \mathcal{E}_2^5(t)\,\mathrm{d}t$	1.3669	1.3668	1.3498
$\frac{1}{T}\int_0^T \mathcal{D}_{\mathrm{E}}^5(t)\,\mathrm{d}t$	0.0021	0.0022	0.0044

Table 4.3: Configuration 3: Time averages of the entropy, turbulent and total energy, as well as the energy defects computed by the LCDCU, LDCU, and VFV schemes.

example. Based on the values reported in Table 4.4, criterion (iii) prioritizes the LCDCU schemes, while the entropy production criterion (i) still prioritizes the VFV schemes.
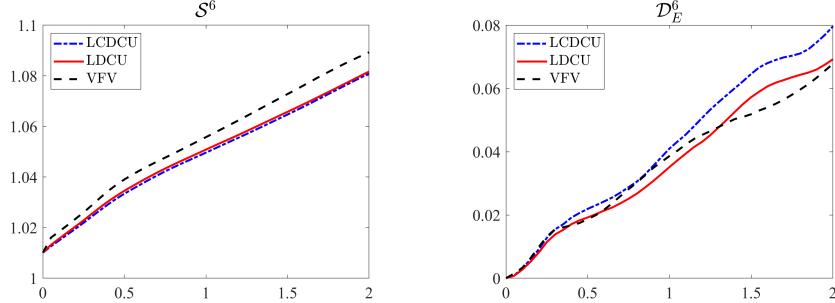
Figure 4.15: KH Instability: Time evolution of the average entropy $\mathcal{S}^6$ (left) and energy defects $\mathcal{D}_{\mathrm{E}}^6$ (right) computed by the LCDCU, LDCU, and VFV schemes.

	LCDCU	LDCU	VFV
$\frac{1}{T}\int_0^T \mathcal{S}^6(t)\,\mathrm{d}t$	1.049343	1.05036	1.05482
$\frac{1}{T}\int_0^T \mathcal{E}_1^6(t)\,\mathrm{d}t$	6.4375	6.4375	6.4375
$\frac{1}{T}\int_0^T \mathcal{E}_2^6(t)\,\mathrm{d}t$	6.3952	6.4003	6.4015
$\frac{1}{T}\int_0^T \mathcal{D}_E^6(t)\,\mathrm{d}t$	0.042321	0.037206	0.036010

Table 4.4: KH Instability: Time averages of the entropy, turbulent and total energy, as well as the energy defect computed by the LCDCU, LDCU, and VFV schemes.

5   Conclusions

In this paper, we have presented a numerical study of dissipative weak (DW) solutions for the Euler equations of gas dynamics. We have considered different benchmark examples, 2-D Riemann problems with continuous or discontinuous solutions, and the Kelvin-Helmholtz (KH) instability problem. Three different numerical methods have been investigated, namely the local characteristic decomposition-based central-upwind scheme (LCDCU), the low-dissipation central-upwind scheme (LDCU), and the viscous finite volume method (VFV). The main result of our numerical study is that different numerical methods may converge to different DW solutions. This fact is evident in the approximation of density and other state variables as well as in the averages over different orders of accuracy, which have been confirmed to converge strongly, even when the convergence of one particular numerical realization is weak only. Furthermore, the averages over different orders of accuracy have been employed to distinguish between weak solutions in the sense of distributions and genuine DW solutions.

We have also computed the approximated error functions for each problem, which, according to our numerical results, behave similarly for different numerical methods. Moreover, we have discovered that the time averages of the average numerical solutions obtained by different methods exhibit similar behavior. In addition, we have approximated the probability density functions of Young measures. In cases where oscillations arise in numerical approximation, the limits are DW solutions and the corresponding Young measures are not Dirac δ-functions and they clearly depend on the scheme. Finally, recognizing that DW solutions are generically not unique, we have explored three potential selection criteria, which are based on the maximization of entropy production and either minimization or maximization of energy defect.

References

[1] R. Borges, M. Carmona, B. Costa, and W. S. Don, *An improved weighted essentially non-oscillatory scheme for hyperbolic conservation laws*, J. Comput. Phys., 227 (2008), pp. 3191–3211.

[2] T. BUCKMASTER, C. DE LELLIS, L. SZÉKELYHIDI, JR., AND V. VICOL, *Onsager's conjecture for admissible weak solutions*, Comm. Pure Appl. Math., 72 (2019), pp. 229–274.

[3] M. CASTRO, B. COSTA, AND W. S. DON, *High order weighted essentially non-oscillatory WENO-Z schemes for hyperbolic conservation laws*, J. Comput. Phys., 230 (2011), pp. 1766–1792.

[4] A. CHERTOCK, S. CHU, M. HERTY, A. KURGANOV, AND M. LUKÁČOVÁ-MEDVIĎOVÁ, *Local characteristic decomposition based central-upwind scheme*, J. Comput. Phys., 473 (2023). Paper No. 111718.

[5] A. CHERTOCK, S. CHU, AND A. KURGANOV, *Adaptive high-order A-WENO schemes based on a new local smoothness indicator*, E. Asian. J. Appl. Math., 13 (2023), pp. 576–609.

[6] A. CHERTOCK, M. HERTY, A. S. ISKHAKOV, A. ISKHAKOVA, A. KURGANOV, AND M. LUKÁČOVÁ-MEDVIĎOVÁ, *Numerical study of random Kelvin-Helmholtz instability*. Submitted. Preprint available at `https://arxiv.org/abs/2511.00008`.

[7] E. CHIODAROLI, C. DE LELLIS, AND O. KREML, *Global ill-posedness of the isentropic system of gas dynamics*, Comm. Pure Appl. Math., 68 (2015), pp. 1157–1190.

[8] S. CHU, Q. FU, M. HERTY, AND A. KURGANOV, *Novel and efficient third-order WENO schemes*. In preparation.

[9] S. CHU, M. HERTY, AND E. F. TORO, *High-order flux splitting schemes for the Euler equations of gas dynamics*, Comput. & Fluids, 300 (2025). Paper No. 106738.

[10] S. CHU, A. KURGANOV, AND R. XIN, *New low-dissipation central-upwind schemes. Part II*, J. Sci. Comput., 103 (2025). Paper No. 33.

[11] S. CHU, A. KURGANOV, AND R. XIN, *New more efficient A-WENO schemes*, J. Sci. Comput., 104 (2025). Paper No. 53.

[12] C. DE LELLIS AND L. SZÉKELYHIDI, JR., *On admissibility criteria for weak solutions of the Euler equations*, Arch. Ration. Mech. Anal., 195 (2010), pp. 225–260.

[13] R. J. DIPERNA, *Measure-valued solutions to conservation laws*, Arch. Ration. Mech. Anal., 88 (1985), pp. 223–270.

[14] W. S. DON AND R. BORGES, *Accuracy of the weighted essentially non-oscillatory conservative finite difference schemes*, J. Comput. Phys., 250 (2013), pp. 347–372.

[15] E. FEIREISL, C. KLINGENBERG, AND S. MARKFELDER, *On the density of "wild" initial data for the compressible Euler system*, Calc. Var. Partial Differential Equations, 59 (2020). Paper No. 152.

[16] E. FEIREISL, M. LUKÁČOVÁ-MEDVIĎOVÁ, B. SHE, AND Y. WANG, *Computing oscillatory solutions of the Euler system via $\mathcal{K}$-convergence*, Math. Models Methods Appl. Sci., 31 (2021), pp. 537–576.

[17] E. FEIREISL AND M. LUKÁČOVÁ-MEDVIĎOVÁ, *Well-posedness of the Euler system of gas dynamics*. Submitted. Preprint available at `https://arxiv.org/abs/2512.18267`.

[18] E. FEIREISL, M. LUKÁČOVÁ-MEDVIĎOVÁ, AND H. MIZEROVÁ, *A finite volume scheme for the Euler system inspired by the two velocities approach*, Numer. Math., 144 (2020), pp. 89–132.

[19] E. FEIREISL, M. LUKÁČOVÁ-MEDVIĎOVÁ, H. MIZEROVÁ, AND B. SHE, *Numerical Analysis of Compressible Fluid Flows*, vol. 20 of MS&A. Modeling, Simulation and Applications, Springer, Cham, 2021.

[20] E. Feireisl, M. Lukáčová-Medviďová, and C. Yu, *Oscillatory approximations and maximum entropy principle for the Euler system of gas dynamics.* Submitted. Preprint available at https://arxiv.org/abs/2505.02070.

[21] U. S. Fjordholm, S. Mishra, and E. Tadmor, *On the computation of measure-valued solutions*, Acta Numer., 25 (2016), pp. 567–679.

[22] Z. Gao, L.-L. Fang, B.-S. Wang, Y. Wang, and W. S. Don, *Seventh and ninth orders alternative WENO finite difference schemes for hyperbolic conservation laws*, Comput. & Fluids, 202 (2020). Paper No. 104519.

[23] S. Gottlieb, D. Ketcheson, and C.-W. Shu, *Strong stability preserving Runge-Kutta and multistep time discretizations*, World Scientific Publishing Co. Pte. Ltd., Hackensack, NJ, 2011.

[24] S. Gottlieb, C.-W. Shu, and E. Tadmor, *Strong stability-preserving high-order time discretization methods*, SIAM Rev., 43 (2001), pp. 89–112.

[25] Y. Jiang, C.-W. Shu, and M. P. Zhang, *An alternative formulation of finite difference weighted ENO schemes with Lax-Wendroff time discretization for conservation laws*, SIAM J. Sci. Comput., 35 (2013), pp. A1137–A1160.

[26] A. Kurganov and E. Tadmor, *Solution of two-dimensional Riemann problems for gas dynamics without Riemann problem solvers*, Numer. Methods Partial Differential Equations, 18 (2002), pp. 584–608.

[27] A. Kurganov and R. Xin, *New low-dissipation central-upwind schemes*, J. Sci. Comput., 96 (2023). Paper No. 56.

[28] K.-A. Lie and S. Noelle, *On the artificial compression method for second-order nonoscillatory central difference schemes for systems of conservation laws*, SIAM J. Sci. Comput., 24 (2003), pp. 1157–1174.

[29] H. Liu, *A numerical study of the performance of alternative weighted ENO methods based on various numerical fluxes for conservation law*, Appl. Math. Comput., 296 (2017), pp. 182–197.

[30] M. Lukáčová-Medviďová, B. She, and Y. Yuan, *What is a limit of structure-preserving numerical methods for compressible flows?*, in European Conference on Numerical Mathematics and Advanced Applications, Springer, 2023, pp. 17–33.

[31] H. Nessyahu and E. Tadmor, *Nonoscillatory central differencing for hyperbolic conservation laws*, J. Comput. Phys., 87 (1990), pp. 408–463.

[32] T. Nonomura and K. Fujii, *Characteristic finite-difference WENO scheme for multicomponent compressible fluid analysis: overestimated quasi-conservative formulation maintaining equilibriums of velocity, pressure, and temperature*, J. Comput. Phys., 340 (2017), pp. 358–388.

[33] J. Qiu and C.-W. Shu, *On the construction, comparison, and local characteristic decomposition for high-order central WENO schemes*, J. Comput. Phys., 183 (2002), pp. 187–209.

[34] C. W. Schulz-Rinne, *Classification of the Riemann problem for two-dimensional gas dynamics*, SIAM J. Math. Anal., 24 (1993), pp. 76–88.

[35] C. W. Schulz-Rinne, J. P. Collins, and H. M. Glaz, *Numerical solution of the Riemann problem for two-dimensional gas dynamics*, SIAM J. Sci. Comput., 14 (1993), pp. 1394–1414.

[36] C.-W. Shu, *Essentially non-oscillatory and weighted essentially non-oscillatory schemes*, Acta Numer., 29 (2020), pp. 701–762.

[37] P. K. Sweby, *High resolution schemes using flux limiters for hyperbolic conservation laws*, SIAM J. Numer. Anal., 21 (1984), pp. 995–1011.

[38] Y. Zheng, *Systems of conservation laws. Two-dimensional Riemann problems*, Progress in Nonlinear Differential Equations and their Applications, Birkhäuser Boston, Inc., Boston, MA, 2001.